Title:

Fast Attentional Information Routing via High-Frequency Bursts in the Human Brain

Authors: Kianoush Banaie Boroujeni[1*], Randolph F. Helfrich[2], Ian C. Fiebelkorn[3], Nicole Bentley[4], Jack J. Lin[5], Robert T. Knight[6], Sabine Kastner[1,7]

Affiliations:

[1]Princeton Neuroscience Institute, Princeton University, Princeton, NJ 08544
[2]Hertie Institute for Clinical Brain Research, Center for Neurology, University Medical Center Tübingen, Tübingen, Germany.
[3]Department of Neuroscience and Del Monte Institute for Neuroscience, University of Rochester, Rochester, NY 14627, USA
[4]Department of Neurosurgery, University of Alabama at Birmingham, Birmingham, Alabama, USA
[5]Department of Neurology, University of California Davis, Davis, CA, USA
[6]Departments of Psychology and Neuroscience, University of California Berkeley, Berkeley, CA, USA
[7]Department of Psychology, Princeton University, Princeton, NJ 08544

*Corresponding author: Kianoush Banaie Boroujeni. Email: kb9590@princeton.edu

Abstract

Brain-wide communication supporting flexible behavior requires coordination between sensory and associative regions but how brain networks route sensory information at fast timescales to guide action remains unclear. Using spiking neural networks and human intracranial electrophysiology during spatial attention tasks, where participants detected targets at cued locations, we show that high-frequency activity bursts (HFAb) serve as information-carrying events, facilitating fast, long-range communications. HFAbs were evoked by sensory cues and targets, dynamically linked to low-frequency rhythms. Notably, both HFAb responses following

cues and their decoupling from slow rhythms predicted performance accuracy. HFAbs were synchronized at the network-level, identifying distinct cue- and target-activated subnetworks. These subnetworks exhibited a temporal lead-lag organization following target onset, with cue-activated subnetworks preceding target-activated subnetworks when the cue provided relevant target information. Computational modeling indicated that HFAbs reflect transitions to coherent population spiking and are coordinated across networks through distinct mechanisms. Together, these findings establish HFAbs as neural mechanisms for fast, large-scale communication supporting attentional performance.

Introduction

Prioritizing information from the external environment to guide ongoing behavior and upcoming actions requires fast coordination of neural activity in large-scale networks distributed across distant brain areas [1–7]. This coordination allows information to be routed selectively from sensory to higher level executive brain networks [8–12]. Previous research, particularly in non-human primates, has shown that selective information routing emerges through dynamically changing neuronal interactions [3,13–15]. Such studies highlight the role of oscillatory dynamics and transient changes in inter-areal coherence in enabling attentional selection and the flexible reconfiguration of neural pathways according to task demands. Yet, most these prior investigations have focused on pairwise interactions between a few brain areas, leaving open the question of how fast neural dynamics emerge and enable flexible, large-scale information routing across distributed networks.

Investigating these questions in the human brain is challenging due to spatial or temporal constraints of the techniques that have been employed. Studies examining network-level interactions have largely been based on connectivity maps derived from functional magnetic resonance imaging (fMRI). While fMRI studies provide valuable insights into functional networks, the temporal resolution cannot capture sub-second routing dynamics in attention tasks [16–20]. Electroencephalography (EEG) and magnetoencephalography (MEG) offer high temporal resolution but have limited spatial resolution. [21,22]. Lastly, single unit recordings provide both fine temporal and spatial signals but lack the broad coverage for addressing questions of brain-wide network communication [3,7,23].

Human intracranial electroencephalography (iEEG), offers a unique opportunity to address these challenges by providing spatially localized and temporally precise neural signals obtained from multiple brain regions [24,25]. High-frequency activity detected in iEEG signals correlates with different cognitive functions, including attention [24–31], and has been reported to index aggregated spiking activity, dendritic post-synaptic activity, state transitions into spiking regimes, or spike current leakage to local field potentials (LFPs) [32–36]. Additionally, high-frequency activities show long-range phase synchronization with different frequency bands, making them candidates for studying fast brain-wide communications [27,37–40]. While these iEEG studies have advanced our understanding of neural communication, they have predominantly focused on interactions between high-frequency activities and low-frequency rhythms (fast-slow interactions), such as cross-frequency coupling, which may not fully capture the dynamics of fast network interactions between high-frequency activities themselves (fast-fast interactions) [27,37,41–45].

Here, we address this gap by identifying transient high-frequency activity bursts (HFAbs) in human iEEG data from epilepsy patients performing spatial attention tasks, hypothesizing that these discrete burst events support fast, large-scale network communications. HFAbs during sensory cue processing predicted successful detection of upcoming targets. They were locally coupled to slow rhythms (4-25 Hz), and transiently decoupled during cue and target processing, with decoupling associated with correct performance. Across the brain, HFAbs interactions were largely characterized by a zero-lag synchronized structure, constituting functionally specialized subnetworks with distinct topographical and temporal organization. Specifically, cue-subnetwork activity preceded target-subnetwork activity following target onset, when sensory cues conveyed relevant information about the target location. Using computational modeling, we then showed that HFAbs likely reflect state transitions in neural populations into a coherent spiking activity state, characterized by bouts of elevated neuronal firing, suggesting HFAbs serve as neural population-level signatures of information-encoding events.

Results

HFAbs track spatial attention and predict behavioral accuracy

We used human iEEG data recorded from epilepsy patients to quantify high frequency activity dynamics to investigate fast information routing. We analyzed data from two spatial attention tasks in which patients were cued either exogenously or endogenously to a spatial location to detect visual targets (**Fig. 1a**, **Extended Data Fig. 1a**). Throughout the paper, the main figures mostly present results of experiment 1, while the results of experiment 2 are presented as supplementary

information supporting reproducibility and generalization across attention tasks (for brain heatmap plots, we combined both experiments to improve 3D rendering coverage).

In experiment 1, patients performed a spatial attention task as described in [29]. Each trial started with the presentation of two vertical or horizontal bar stimuli. Patients were instructed to fixate their gaze at the center of the display. A transient spatial cue appeared at the end of one bar, exogenously cueing an upcoming target location. Following a delay period, a target (i.e., luminance changes at perceptual threshold) appeared at the cued location or infrequently at equally distant non-cued locations. Patients were required to respond if they detected the target (**Fig. 1a**). In experiment 2, patients were endogenously cued to a hemifield and reported a target if it appeared in the cued hemifield (**Extended Data Fig. 1a**, see **Methods,** and for more details see [4]). First, we used an adaptive method [7] and detected reliable bursts of high frequency activity at each electrode (HFAbs, 65-115 Hz, intermittent high amplitude oscillatory events lasting more than 2.5 frequency cycles (> 25 ms), average burst length 36.2 ms; **Fig. 1b**). The frequency band was selected based on average spectral peaks observed across subjects (91.2 ± 20.9 Hz , n = 12, see **Methods** for further details). We then calculated the HFAb density (number of HFAb events per unit of time) for each electrode to examine their evoked response during different task epochs. HFAbs showed higher density averaged across all electrodes in response to both cue and target (**Fig. 1c, Extended Data Fig. 1b**). We measured HFAb responses following cue and target onsets across different trial outcomes (hit, reject, miss, and false alarm). At the population level, HFAbs activated to cue onsets in correct hit and reject trials (Wilcoxon signed-rank test, $P < 0.001$) and differed significantly from missed and false alarm trials (Kruskal-Wallis test, $P = 0.001$, Dunn's test, $P = 0.008$ and $P = 0.01$, respectively; **Fig. 1d**). Target responses were also significantly different in correct hit trials compared to other outcome conditions (Kruskal-Wallis test, $P < 0.001$;

Dunn's test, $P < 0.001$; **Fig. 1d**, **Extended Data Fig. 1c**; see also **Extended Data Fig. 2a, 1d**). Overall, 10.7 ± 2% of channels (n = 12) showed significant activation to cues, whereas 33.2 ± 3% of channels (n = 12) were responsive to targets (Wilcoxon signed-rank test, $P < 0.05$). Among channels that responded to cues and/or targets, HFAb responses to targets were negatively correlated with those to the cue (Spearman correlation, $P < 0.001$, $R = -0.36$, **Fig. 1e**), suggesting distinct electrode populations process cues and targets. The topography of burst responses to cues was largely confined to occipital and parietal regions, including areas in extrastriate cortex, intraparietal sulcus (IPS), temporoparietal junction (TPJ), superior parietal lobule (SPL), and inferior parietal lobule (IPL) (**Fig. 1f**), whereas target responses were more widely distributed including superior, middle, and inferior frontal gyrus, precentral and postcentral gyrus, IPL, SPL, and TPJ (**Fig. 1g**). This activation profile was evident only for correct trials both for cue- and target responses (**Extended Data Fig. 2b**). HFAb responses for correct and incorrect trials also showed topographic differences at the single subject level (**Fig. 1h**, see **Extended Data Fig. 1e, 2c** for more individual examples; also see **Supplementary Table 1** for detailed electrode positions of cue and target responsive channels for individual subjects).

We investigated the effect of cue validity (targets at cued vs uncued location) and laterality (visual field ipsilateral versus contralateral to electrodes) on cue and target responses on a trial-by-trial basis, using a Generalized Linear Mixed Effect (GLME) model (see **Methods**). Overall, there was a main effect of outcome on both cue response ($t = 2.8$, $P = 0.005$) and target response (GLME, $t = 15.2$, $P < 0.001$). Additionally, there was a main effect of cue validity on the target response (**Fig. 1i**, GLME, $t = 4.7$, $P < 0.001$), and a main effect of the cue laterality on the cue response (**Fig. 1j**, GLME, $t = 5.1$, $P < 0.001$). No significant main effect was observed for laterality on target response (**Extended Data Fig. 3a**, $P = 0.13$), or validity on cue response (**Extended Data Fig. 3B**,

P = 0.32, See **Extended Data Fig. 3c,d** for the effect of laterality and cue validity on cue and target response in experiment 2, as well as **Extended Data Fig. 3e,f** for the temporal profiles of HFAbs around cue and target onsets in both experiments).

Given that HFAb activation to sensory cues was associated with outcome accuracy, we examined if electrode burst density (Cue+ electrodes, see **Methods**) predicted whether participants successfully completed a trial (correct hits and correct rejections). We trained a classifier on the burst density using a sliding window of 350 ms around the cue onset. In Cue+ electrodes and within 500 ms after the cue onset, the burst density predicted better than baseline and chance levels if the trial was executed correctly (binomial test, FDR corrected for dependent samples, $P < 0.05$, **Fig. 1k, Extended Data Fig. 3g**). This prediction was consistent across both experiments (**Extended Data Fig. 3h**) and was not dependent on an individual subject (**Extended Data Fig. 3i**).

These findings indicate that HFAbs occur frequently in response to sensory cues and targets and exhibit distinct spatial profiles across the brain. HFAbs predicted performance accuracy following the cue-onset on a trial-by-trial basis. These results support a role for HFAbs in encoding spatially relevant sensory information for subsequent target detection.

HFAbs are coupled to slow rhythms and decouple in response to cues and targets

High frequency activity dynamics in brain networks have been shown to be organized by theta rhythms (4-8 Hz) [37]. Here, we asked whether HFAbs are coordinated with low-frequency rhythms, and whether these cross-frequency dynamics were associated with task variables. For each electrode, we extracted the LFP around the HFAb centers and measured both the HFAb-triggered LFP average and the phase locking value (PLV) of HFAbs (peak time) to the low-frequency LFP

dynamics. HFAb-triggered LFP showed consistent evoked potentials with low frequency side-lobes across all subjects (**Fig. 2a**). Spectral analysis revealed HFAb-triggered spectral peaks (**Fig. 2b**, top) and phase locking peaks (**Fig. 2b**, bottom) in theta (4–8 Hz), alpha (8–14 Hz), and beta (15–25 Hz) frequency bands. Phase locking to local low-frequency field dynamics was evident in most electrodes across all subjects (**Fig. 2c,** 9 ± 0.24 Hz**,** with significant peaks marked by black dots; see **Fig. d, Extended Data Fig. 4c** for examples of individual electrodes showing phase distributions of HFAbs locked to one or more frequency bands, also see **Extended Data Fig. 4a,b** for topographic representations of the frequency of phase locking peaks at the group and individual levels).

To examine whether sensory cues or target processing affected HFAb phase locking to low-frequency rhythms, we analyzed PLV of HFAb relative to baseline following cue and target onsets. HFAbs showed a transient decrease in their phase locking (decoupling) with the theta/alpha and beta frequency bands after the cue onset and after the target onset (**Fig. 2e, Extended Data Fig. 4d,** randomization test, $P < 0.05$, FDR corrected for dependent samples). This decoupling was not attributable to event-triggered potentials (**Extended Data Fig. 4e**, see **Methods**). Furthermore, changes in HFAb coupling strength were only observed in correct trials, not in incorrect trials (**Fig. 2f,g,** number of bursts were controlled across trial conditions, see **Methods**, see **Extended Data Fig. 4f** for individual examples).

Next, we examined whether alterations in HFAb coupling to low frequencies were related to HFAb activation profiles in response to cues and targets. We calculated correlations between coupling ratios and burst density for each subject (a coupling ratio measured changes in HFAb coupling to low frequencies (< 25 Hz) after cues or targets relative to the baseline within 1000 ms before the cue and target onset, see **Methods**). The coupling ratio at target and cue onsets was negatively

correlated with burst density for both cue and target onsets (**Fig. 2h,i**, Spearman correlation, R = -0.22, $P < 0.001$, and R = -23, $P<0.001$). GLM models showed a main effect of cue response on the coupling ratio following cue onset (**Fig. 2h** t = -6.17, $P < 0.001$), and a main effect of target response on the coupling ratio following target onset (**Fig. 2i,** t = -5.05, $P < 0.001$). No significant effect of cue response was found on the coupling ratio following target onset (**Extended Data Fig. 4h,** P = 0.15), and target response on the coupling ratio following cue onset (**Extended Data Fig. 4i,** P = 0.21).

Overall, HFAbs were predominantly coupled to the phase of theta, alpha, and beta rhythms. However, their coupling strength to slower rhythms decreased during perceptual processing and decision making.

HFAbs were coordinated brain-wide and their network-level synchronization identified functionally specialized subnetworks

We found that HFAbs evoked by cue and target demonstrated different topographical distributions, indicating that different brain regions are preferentially engaged during cue and target processing. Additionally, the processing of cues and targets involved the decoupling of HFAbs from low-frequency dynamics. The distinct spatial patterns and reduced low-frequency coupling suggest that separate groups of brain areas (subnetworks) are coordinated via HFAbs for cue versus target processing. Thus, we asked whether the brain-wide network could be organized into distinct subnetworks, each characterized by unique high frequency coordination patterns.

We analyzed burst events outside the cue/delay and target/response periods to avoid stimulus-driven coordination effects. We measured the power of high frequency activity (65-175 Hz, HFA, to capture broader spectral contents) in one electrode aligned to the center of HFAb events in

another electrode (HFAb-triggered HFA). HFAb-triggered HFA between electrodes revealed coordination in high frequency bands (**Fig. 3a**). This coordination was organized through low frequency rhythms, with spectral peaks predominantly in the theta band (4-8 Hz) (**Fig. 3b**, top). These patterns were consistent across subjects and experiments (**Fig. 3b**, bottom, **Extended Data Fig. 5a,b**). HFAb coordination strength (the sharpness of HFAb-triggered HFA) was inversely related to distance between electrodes, with closer sites showing stronger coordination (**Fig. 3c**, **S5e**, Spearman correlation between coordination kurtosis and distance between electrodes, $R = -0.25$, $P < 0.001$).

To extract temporal features of the high frequency coordination, we used Principal Component Analysis (PCA) to reduce the dimensionality of HFAb-triggered HFA across electrode pairs. The first component (PC1) showed zero-lag synchronized and near-symmetric distributions of high frequency activity in all subjects, explaining more than 20% of the total variance (**Fig. 3d, Extended Data Fig. 5d,e**). We projected HFAb coordination onto PC space and used a resampling-based consensus K-means clustering technique to identify robust subnetworks of electrodes based on their scores on the synchronized PC (**Extended Data Fig. 5f**, see **Methods**). The clustering algorithm identified the most stable subnetworks (electrodes that were consistently grouped together across multiple resampling runs) for each cluster number ($K = 2$-8, see **Extended Data Fig. 6a**, **7a** for individual examples). We defined a series of accuracy metrics and determined the optimal number of clusters through a voting poll over those metrices for each subject (the cluster number that outperformed the other clusters in more of these metrics) (**Extended Data Fig. 6b,c** and **Extended Data Fig. 7b,c,** see **Methods**). An example clustering result with eight optimal clusters is shown in **Fig. 3e** (see **Extended Data Fig. 8** for additional examples).

Next, we investigated whether these clusters were functionally specialized. All subjects (except one excluded due to insufficient electrodes) showed clusters with distinct cue- and target-evoked activation profiles (**Fig. 3f,** see **Extended Data Fig. 9** for activation profiles for different cluster numbers for the individual shown in **Fig. 3e**, also see **Extended Data Fig. 6d** and **Extended Data Fig. 7d** for additional examples). Clusters activated by cues and targets were labeled as *cue-* or *target-subnetworks*, respectively (Wilcoxon signed-rank test, $P < 0.05$; FDR corrected for dependent sample). Cue-subnetworks were predominantly located in occipital and parietal cortices (e.g., IPS, TPJ, SPL, IPL), while target-subnetworks were more widely distributed across different brain areas including parietal, motor, premotor, and frontal cortices (**Fig. 3g**, see **Supplementary Table 2** for locations of cue and target subnetworks for individual subjects).

Lastly, similar to **Fig. 1h**, we tested whether cue and target-subnetworks could predict trial outcomes. The density of HFAb within 98-374 ms after sensory cues predicted successful detection of upcoming targets (binomial test, $P < 0.001$, FDR corrected for dependent samples). This prediction was only true for the cue-subnetwork (**Fig. 3h**) and was not driven by a single subject (see **Extended Data Fig. 10** for more details on the classifier results in both experiments). As a control, we re-referenced datasets from common average referencing to local composite referencing (LCR, each electrode was referenced to its nearest neighbors, see **Methods**), This re-referencing did not alter any of the main results. Together, these findings suggest that large-scale brain networks are coordinated via HFAbs, with their synchronization identifying functionally specialized subnetworks that exhibit distinct temporal dynamics. Furthermore, HFAbs in subnetworks activated by sensory cues were predictive of performance accuracy following cue onsets.

HFAbs in cue-subnetworks precede target-subnetworks

Our observation that HFAb responses in cue-subnetworks predict performance suggests that these subnetworks play a critical role for successful target detection. This finding raises a key question: do cue-subnetworks actively route information to target-subnetworks during target processing? If so, this would imply a directional flow of information between these subnetworks that facilitates attentional performance. To address this question, we examined information flow between cue and target-subnetworks. We only considered subjects whose electrode coverage included both cue- and target-subnetworks ($n = 6$). We used two different approaches. First, we quantified whether HFAbs exhibited any temporally ordered activity pattern during the target-to-response period between cue and target-subnetworks. Individual subjects showed stronger HFA in target-subnetworks within 150 ms after HFAbs in cue-subnetworks (**Fig. 4a, Extended Data Fig. 11a,** Wilcoxon rank-sum test, $P < 0.05$, the opposite pattern was observed in the other direction). On average, HFAbs in cue-subnetworks led the activity of target-subnetworks and target-subnetworks lagged cue-subnetworks during the target processing period (within 150 ms around the HFAb-triggered HFA, Wilcoxon rank-sum test, $P < 0.001$, **Fig. 4b).** For comparison, no lead-lag patterns were observed between cue- and target-subnetworks during the cue-to-target interval **(**$P = 0.44$, n.s., **Extended Data Fig. 11b).** We quantified the peak of these lead-lag relationships for individual subjects. The HFA in target-subnetworks showed an activity peak following HFAbs in cue-subnetworks, while the peak of HFA in cue-subnetworks preceded HFAbs in target-subnetworks (**Fig. 4c**, Wilcoxon rank-sum test, $P < 0.05$, 16 ± 7 ms; $n = 6$). For visualizing the lead/lag pattern in each individual, we averaged the time-lags between cue and target-subnetworks over different cluster numbers. We observed that the HFAbs in the occipital, posterior parietal, and frontal areas led over the

motor/premotor areas during target processing (**Fig. 4c**, see **Extended Data Fig. 11c** for more examples).

Next, we used delayed mutual information (DMI) to further quantify how information was directionally coupled between cue and target-subnetworks. DMI can inform about (i) when cue and target-subnetworks shared the most information relative to target onset, and (ii) the specific time-lags at which these two subnetworks showed maximum inter-predictability (see **Fig. 4e** for an individual example).

The DMI between cue and target-subnetworks showed a peak up to 500 ms after target onset (**Fig. 4f,** 275 ± 22 ms; n = 6). Time-lag distributions of the maximum DMI between cue and target-subnetworks showed that cue-subnetworks preceded the information in target-subnetworks during the target processing period (**Fig. 4f,** Wilcoxon signed-rank test, $P < 0.001$; 67 ± 16 ms, n = 6). This pattern was consistent for individual subjects (**Fig. 4e,g**, see **Extended Data Fig. 11d** for more examples) as well as on an average group level (**Fig. 4f**). The information precession in cue-subnetworks over target-subnetworks was only evident after the target onset. No significant time-lag was observed around the cue onset, indicating this effect is not a reflection of visual hierarchy activation (**Extended Data Fig. 11e**). This effect was limited to trials with a valid sensory cue, where the target appeared as instructed by the visual cue (**Fig. 4g**).

Overall, these results suggest that brain subnetworks, identified by their network-level HFAb synchronization, exhibit temporal lags during different functional states. Specifically, when the cue provides valid spatial information about the target, HFAbs in cue-subnetworks precede those in target-subnetworks following target onset.

Computational modeling of HFAbs through spiking neural networks

We developed a computational model using spiking neural networks [46] to gain mechanistic insights into HFAbs, their dynamic coupling to low-frequency rhythms, and their coordination across brain networks. We simulated two interconnected networks, each consisting of 1000 neurons (80% excitatory, 20% inhibitory; **Fig. 5a, Extended Data Fig. 12a,** see **Methods**). Each network was fed by external input currents primarily to the excitatory population.

We implemented two recording sites on top of each network measuring electrical field dynamics of postsynaptic and transmembrane potentials from all neurons in that network (**Fig. 5a)**. A non-ohmic filter was used to attenuate higher frequencies in the iEEG signal (**Fig. 5b**, **Extended Data Fig. 12b,c** see **Methods**). Simulated iEEG signals showed low-frequency spectral peaks corresponding to network resonance frequencies and high frequency (65–115 Hz), consistent with experimental data (**Fig. 5c**). HFAbs were detected as transient oscillatory events of high amplitude at 65-115Hz (**Fig. 5d**).

To investigate the neural mechanisms underlying these HFAbs, we calculated the spike density for the population of neurons, and the HFAb density from each recording site. Burst density correlated with spike density as compared to bursts with random timings (randomization test, $P < 0.05$, **Fig. 5d**). This was further quantified by feeding the network different levels of external current coherence (**Extended Data Fig. 12c)**. Increasing the input coherence to the network showed a linear increase in correlation between the HFAb density and the spike density (Spearman correlation, $R = 0.87$, $P < 0.001$, **Fig. 5e**). This observation is consistent with our experimental findings that HFAbs are evoked in response to cues and targets, suggesting that they may reflect large-scale information-carrying events emerging from transiently elevated excitation in local networks of neurons.

Next, we examined HFAbs coordination with slower rhythms. HFAb-triggered LFPs at each recording site showed an evoked responses with low-frequency sidelobes (**Fig. 5f**), revealing spectral peaks in low frequencies (< 25 Hz) as well as the burst frequency band (**Fig. 5g**). The cross-spectral correlation was dependent on synaptic time constants, external input strength, neural connectivity strength, and coherent input consistency (**Fig. 5g**). HFAbs also showed phase locking to different frequencies in the theta, alpha and beta bands (4-25 Hz, **Fig. 5h**). These results are consistent with the prominent local cross-spectral coupling observed in our experimental data, supporting local neural network mechanisms underlying the coupling of high- and low-frequency dynamics.

We also tested for possible network mechanisms underlying the decoupling following cue and target processing. We modeled this scenario through feedforward networks and measured the time-resolved PLV for both networks after feeding one with a brief input pulse (~50% of neurons receiving in-phase inputs; **Fig. 5i, Extended Data Fig. 12e,f**). The external impulse desynchronized both networks, resulting in a transient decoupling of HFAb from low-frequency rhythms as compared to the baseline (Wilcoxon rank-sum test, $P < 0.001$, **Fig. 5i, Extended Data Fig. 12g,h**). This desynchronization was accompanied with higher burst rate (**Extended Data Fig. 12i)**.

Lastly, we examined HFAb coordination across networks. HFAb-triggered HFA showed different rhythmically organized coordination patterns between networks depending on inter-network connectivity and external inputs. Reciprocally connected networks and networks with correlated external inputs showed synchronized high frequency activity (**Fig. 5j**), while feedforward networks showed a lead-lag pattern within 150 ms following HFAbs (Wilcoxon rank-sum test, $P < 0.001$, **Fig. 5k**). In addition to the internally generated rhythmic structure of HFAbs between

346 networks, external inputs may also contribute to these rhythmic coordination patterns. A rhythmic
347 input to either or both networks entrained its rhythm in the coordination of HFAbs between the
348 two networks (Spearman correlation, $R = 0.83$, $P < 0.001$, **Fig. 5l,m**).
349 In sum, our modeling results suggest that HFAbs reflect a transition in neural populations into a
350 state of coherent spiking activity. These HFAbs are phase locked to low-frequency rhythms, but
351 transient inputs disrupt this coupling. HFAbs are coordinated across interconnected networks or
352 networks as a function of task structure.
353

354 **Discussion**

355 Here we present a novel framework for understanding the mechanisms underlying large-scale
356 information routing in brain networks at fast timescales. By characterizing high-frequency
357 activities as discrete burst events (HFAbs), our study identified brain subnetworks with similar
358 coordination patterns, which tracked the encoding and communication of spatially relevant sensory
359 cue information within large-scale brain networks. We found that HFAbs were predominantly
360 synchronized across distributed brain networks in iEEG data, and their network-level
361 synchronization patterns revealed functionally specialized subnetworks for processing cues and
362 targets. Importantly, HFAbs in cue-subnetworks following sensory cues predicted trial-by-trial
363 performance accuracy, and temporally preceded the activity of target-subnetworks during
364 subsequent target processing, highlighting their role in dynamic attentional information routing.
365 Using computational modeling, we then showed that HFAbs can emerge as bouts of elevated
366 excitatory drive to local networks, functioning as fast communication units across the brain. These
367 findings demonstrate that HFAbs are involved in both forming a brain-wide representation of

sensory cues and fast communication of these sensory signals to associative brain networks for detecting upcoming targets and decision-making processes.

High-frequency activity have been widely observed in human intracranial recordings and is associated with a wide range of cognitive and circuit functions [24,25,27,31,37,38,44]. Instead of continuous measures, we characterize these activities as discrete burst events, supported by computational and animal electrophysiology studies emphasizing their circuit-level origins and their essential roles in long range communications [7,47–53]. Through this quantification, we demonstrated that HFAbs can leverage our understanding of fast attentional information routing in large-scale brain networks. Previous studies investigating neural mechanisms of selective attention have predominantly focused on pairwise interactions between brain regions, often measured by coherence of neural signals in lower frequency bands [3,54]. This pairwise perspective on neural communication does not fully capture the complexity of brain-wide network dynamics essential for a detailed and mechanistic view of cognitive functions [20,55]. By utilizing HFAbs, our results offer a large-scale account for understanding information routing and communication at millisecond timescales at the network level, providing new insight into the mechanisms of selective attention.

A main finding of our study revealed the synchronized inter-regional temporal structure of network coordination through HFAbs. We found that the most prominent pattern of high frequency dynamics in the brain network was zero-lag amplitude synchronization (**Fig. 3d**). This long-range synchronization of HFAbs is consistent with previous studies showing phase locking of high frequency dynamics in brain networks [38–40]. Zero-lag synchronization patterns in cortical networks

are thought to enhance large-scale information processing and facilitate representational states of sensory information in the brain [2,56–58]. While our results cannot directly identify the origins of these synchronized interactions, two different scenarios might be involved. One potential synchronizing mechanism may rely on subcortical areas [59–63], particularly higher-order thalamic nuclei [59,64–67]. Our modeling suggests that correlated inputs to distinct neural networks could drive long-range synchronization (**Fig. 5l**). Such correlated inputs, if originating from subcortical structures such as higher-order thalamic nuclei, can facilitate the long-range synchronizations between separate or weakly connected cortical areas [59,68]. Another potential mechanism would depend on direct long-range intracortical interactions. We found that cortical synchronization was largely between areas with similar activation profiles during cognitive functions and spatially neighboring regions (**Fig. 3, Extended Data Fig. 8**). Additionally, our modeling suggested that reciprocally connected networks with similar connectivity strength can result in synchronized dynamics (**Fig. 5j**). This zero-lag synchronization induced by reciprocal connections has been observed experimentally in long-range neuronal interactions [56,57] as well as in network modeling [69]. Recent findings in mice support this idea reporting that deep layer 6b neurons, which are recipient of long-range cortical projection neurons [70], are involved in brain state shifting into a spiking state, and strong high frequency activity (80–140 Hz); in brain networks [36]. While our modeling and empirical results can support either of these mechanisms, future studies are needed to explore the extent to which cortico-cortical versus thalamocortical interactions drive and influence this high frequency synchronization in large-scale cortical networks.

We further showed that network-level baseline synchronization of high-frequency dynamics, outside of task events, can reliably identify distinct functional brain subnetworks through a resampling-based consensus clustering framework. While the baseline state did not contain cue or

target processing periods, it could identify subnetworks with unique activation patterns in response to those behavioral events (**Fig. 3**). It is notable that this approach fundamentally diverges from the most common ones taken to delineate brain network organizations or network-level communications such as conventional fMRI that is primarily focused on low-frequency BOLD signal fluctuations [71–73]. By leveraging high-frequency dynamics, we show a novel link between baseline neural activity and task-induced network activation patterns, suggesting that intrinsic network fluctuations can affect behavioral responses even at millisecond timescales. Identifying these subnetworks at fast time scales is critical to capture rapid state transitions in brain networks, which may underlie the temporal organization necessary for adaptive information routing during behaviorally relevant events [74]. This capacity is reflected in our findings, which reveal that brain subnetworks, identified by their fast, network-level synchronization, exhibit lead-lag interactions during behavioral events. Specifically, cue-subnetworks led target-subnetworks during target presentation when spatial cues provided relevant information about target locations (**Fig. 4**). These observations uniquely bridge the gap between studies focusing on local and cross-regional mechanisms of fast information routing [7,44,48,50,52,64,75] and those examining communication in large-scale brain networks beyond pairwise interactions [20,76,77].

Another key observation in this study is the coupling dynamics of HFAbs and local low-frequency activities. We found that the phase-locking of HFAbs to low-frequency dynamics can occur with random external input patterns in the modeling, and this is a widespread phenomenon in iEEG signals, consistent with previous studies [37,78,79]. However, our findings further suggest that HFAbs transiently decouple from the phase of local low-frequency activities in response to both cue and target events (**Fig. 2**). Our modeling supports this observation, showing that transient inputs,

whether directly fed into a network (e.g., a visually evoked response from subcortical structures) or indirectly through a feedforward structure, can interrupt the default state coupling of HFAbs to low frequencies (**Fig. 5i**). Network interferences, characterized by brief and strong responses, can temporarily induce local cross-frequency decoupling possibly by increasing response heterogeneity and disrupting the timing of inhibitory and excitatory neuron activation [80,81]. This desynchronization can facilitate cognitive processes like selective attention, perception, and memory retrieval by enhancing new information and suppressing internally regulated activity states [80,82–86]. We observed that HFAb decoupling from low-frequency dynamics, accompanied by increased HFAb density following cue and target events, resembling a desynchronized up-state, which is a brain state with activated but desynchronized neural activity across cortical networks. Importantly, this decoupling was more pronounced in correct trials during both cue and target processing, further suggesting a role of desynchronization in facilitating accurate cognitive performance (**Fig. 2g**).

In summary, our study provides a novel approach to understanding large-scale cortical communications, showing that HFAbs act as fast communication units in the brain, supporting long-range information processing, facilitating attentional information routing, and identifying distinct and functionally specialized brain subnetworks.

Acknowledgments

This work was supported by the C.V. Starr Fellowship (KBB), German Research Foundation, Emmy Noether Program (DFG HE8329/2-1; RFH), NINDS (R01NS021135; RTK), and NEI (2R01EY017699; SK), NIMH (2R01MH064043, P50MH109429; SK). The funders had no role

459 in study design, data collection and analysis, the decision to publish, or the preparation of this
460 manuscript.
461
462
463
464 **Author Contributions**
465 Conceptualization, K.B.B. and S.K.; Methodology, K.B.B.; Formal Analysis, K.B.B.;
466 Investigation, R.F.H., and J.J.L.; Software, R.F.H. and I.C.F.; Visualization, K.B.B; Writing –
467 Original Draft, K.B.B.; Writing – Review & Editing, K.B.B., R.F.H., N.B., R.T.K., and S.K..;
468 Supervision, S.K.
469
470 **Data and code accessibility**
471 Custom programming code for analysis and modeling is available upon publication and will be
472 deposited in an online directory.
473
474 **Competing Interest**: The authors declare no competing interests.
475
476

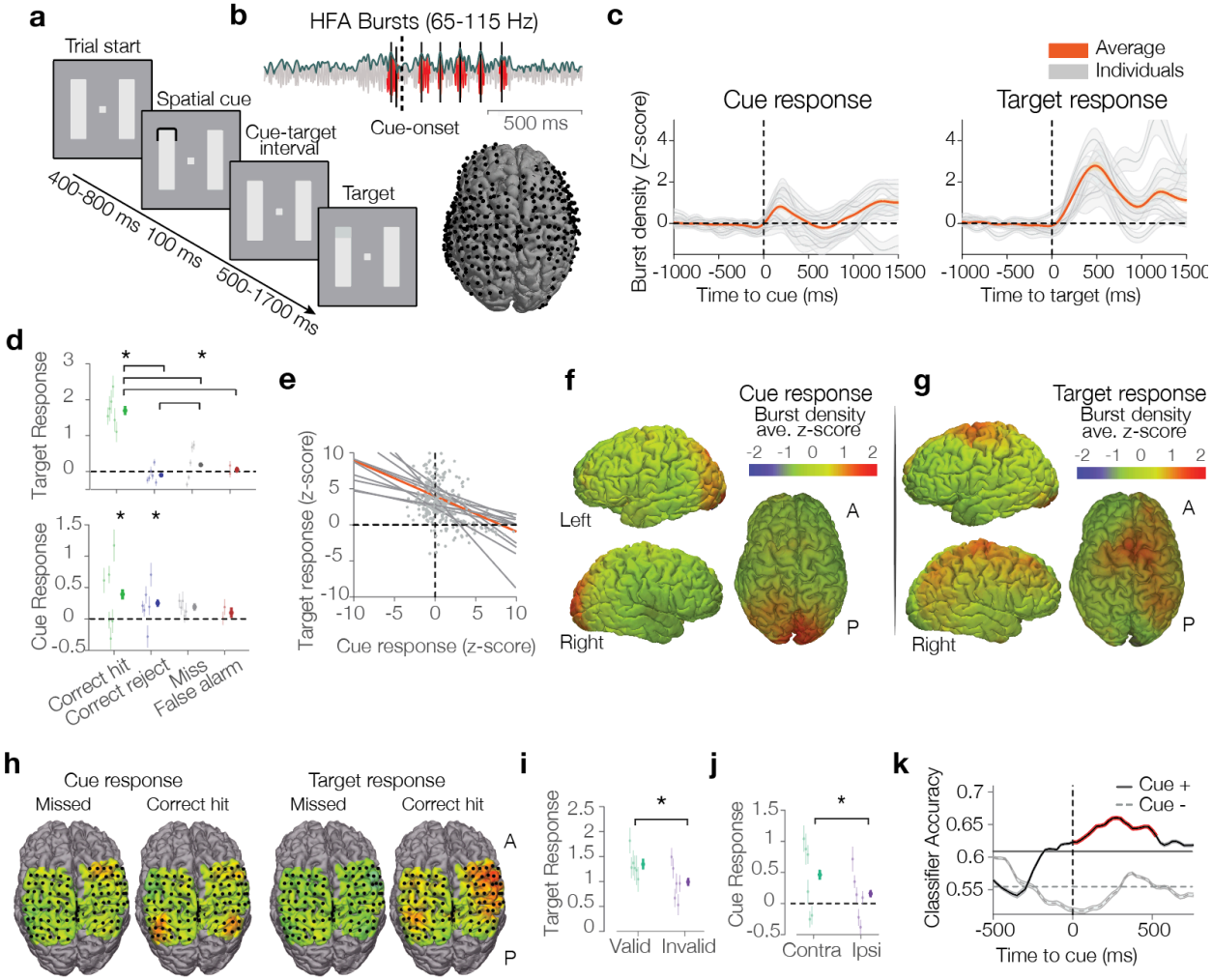

Fig. 1. HFAb activation profile predicts behavioral outcome on a trial-by-trial basis. a, A schematic of experiment 1 task outline. Two bars appear on the screen. A transient cue informs the subject of the most probable location of an upcoming target. A target at perceptual threshold contrast change appears at a cued or infrequently at an equidistant uncued location after a variable interval. Subjects report the change detection. **b**, An example trial of detected transient high-frequency bursts (HFAbs, shown in red) around the cue onset. The brain shows localization of electrodes across all subjects. **c**, Normalized HFAb density profiles for individual subjects and averaged across participants aligned to the cue (left) and target onset (right). **d**, HFAb responses to cues (left) and targets (right) grouped by trial outcome. (Each line represents one subject, with thick lines showing group average, horizontal lines showing significant differences between groups, and asterisks denoting non-zero responses). **e**, Correlation of HFAb responses evoked by cue and target onset for channels with significant activation to either or both cue and target (each point represents one channel, each line represents regression for one subject, the orange line shows regression across all channels). (**e, g**) Group average heatmap 3D rendering of HFAb responses to (**a**) cues and (**g**) targets for correct trials. **h**, An individual subject example of HFAb responses to cue and target within 500 ms after the cue and target onset, respectively, for correct and incorrect trials (black circles indicate electrode locations). **i**, HFAb responses to targets for valid and invalid

cue conditions. **j**, HFAb responses to cues ipsi- and contra-lateral to electrodes. **k**, Classifier accuracy in predicting trial outcome based on HFAb density around the cue onset for cue responsive electrodes and cue unresponsive electrodes (error bars indicate standard error of the mean across all realizations and cross validations). Red lines indicate significantly higher prediction accuracy than baseline and chance levels ($P < 0.05$, binomial test, FDR corrected for dependent samples).

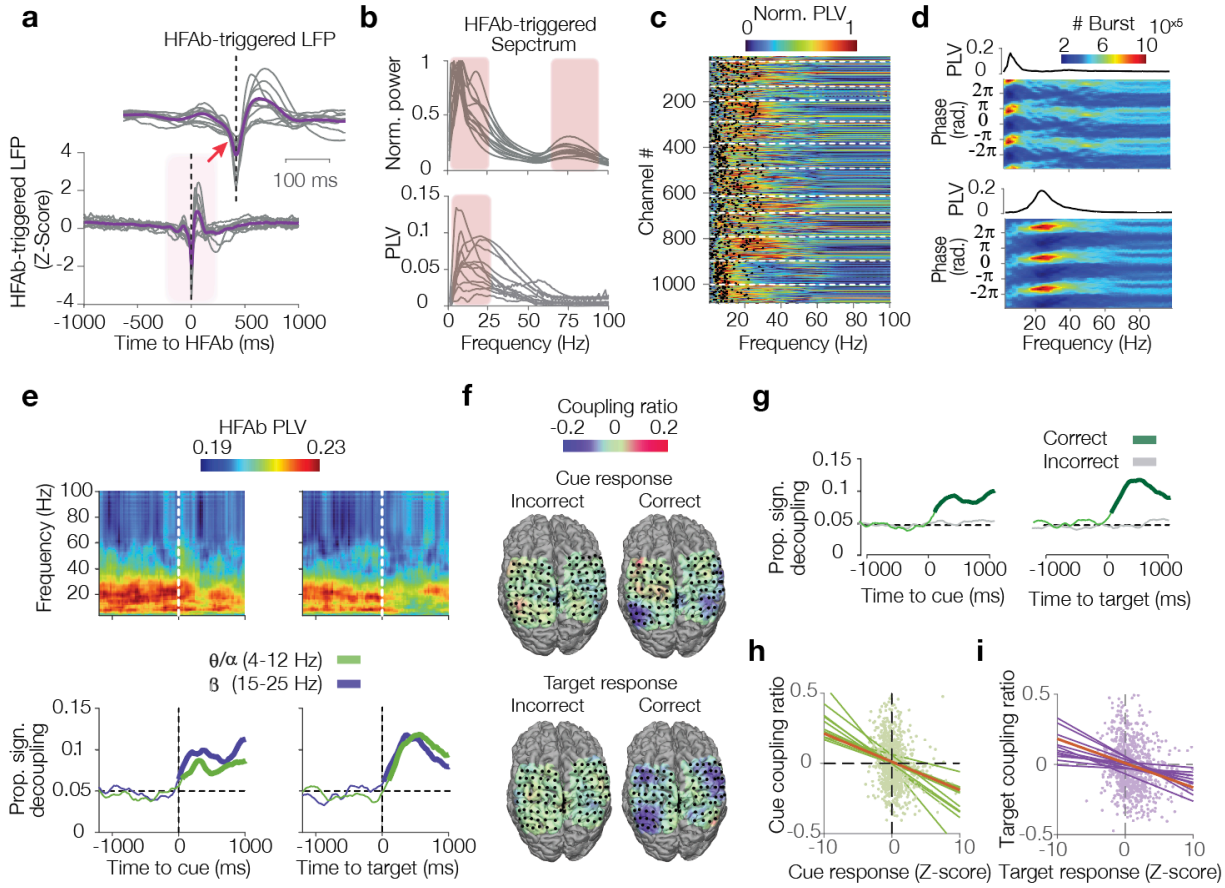

Fig. 2. HFAbs dynamically phase lock to low-frequency LFPs and decouple transiently after cue and target onsets. a, HFAb-triggered LFP averages across all electrodes for individual subjects (gray lines) and across all individuals (purple line). **b**, HFAb-triggered LFP spectrum (top) and phase locking values (PLV, bottom) across all electrodes (each line represents one subject). **c**. PLVs for individual electrodes (each row)**.** Black dots indicate the maximum peak of PLV for each electrode, and white dashed lines delineate results from individual subjects. **d**, Example of phase-frequency distribution of HFAbs for an electrode with theta phase locking (top) and beta phase locking (bottom). **e**, Time-resolved PLV analysis averaged across all subjects (top) aligned to cue (left) and target (right) onsets. The proportion of time points where phase locking dropped significantly below the baseline averaged across all electrodes (bottom, $P < 0.05$, random permutation test; thick lines indicate segments significantly different from the chance level, $P < 0.05$, binomial test, FDR corrected for dependent samples; see **Methods**). **f**, An individual brain heatmap example showing coupling ratio between HFAb and low frequency (4-25 Hz) LFP after cue (top) and target onsets (bottom) for correct and incorrect trials. **g**, Similar to **f**, proportion of time points with significant decoupling from low frequency LFPs (4-25 Hz) after cue and target onsets for correct and incorrect trials. (**h, i**) Regression plots showing correlation of coupling ratios following cue onset with cue responses (green, **h**), and coupling ratios following target onset with target responses (purple, **i**). Scatter points denote electrodes, lines indicate individual subjects with orange line showing the regression across all subjects.

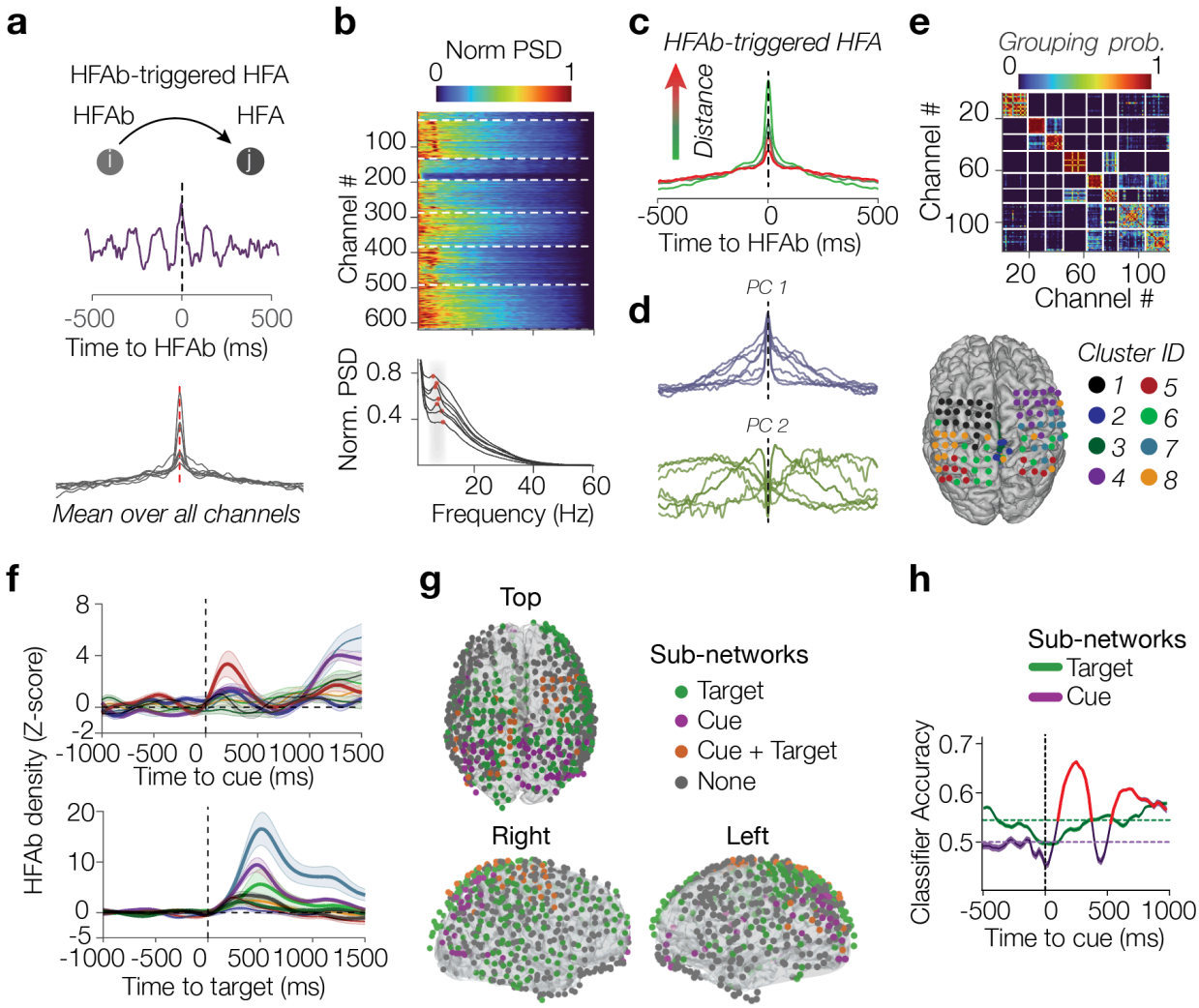

Fig. 3. Long-range coordination of HFAbs identifies functionally specialized subnetworks. a, High frequency coordination was measured by calculating HFAb-triggered HFA between electrode pairs for HFAbs outside of cue/delay and target/response periods (top shows an electrode pair example, and bottom shows HFAb-triggered HFA averaged over all electrode pairs for individual subjects). **b**, Normalized PSD over HFAb-triggered HFA for all electrodes (each electrode relative to the rest of the network; white dashed lines are the border between subjects)**. c**, HFAb-triggered HFA for electrodes distanced in four quantiles (25, 50, 75, and 100 mm), from green (short) to red (long). **d**, The first two principal components of HFAb-triggered HFA for individual subjects. **e**, A pair-wise grouping probability matrix for an individual example with an optimal number of eight clusters (top, white lines indicate cluster borders, clusters are ordered from top to bottom by their stability, see **Methods**). Cluster topography for the K = 8 number of clusters for an individual subject shown in (bottom). **f**, Normalized burst densities around cue and target onsets averaged across electrodes within each cluster for the same subject as in **e**. (shaded error bars indicate the standard error of the mean; significant activations are indicated by thicker lines, $P < 0.05$, Wilcoxon test). **g**, Topographical organization of electrodes in clusters that show significant activation in response to cues and targets across all subjects (i.e., "cue-subnetworks" and "target-subnetworks"). **h**, Classifier accuracy based on HFAb density around cue onset for

cue-subnetworks (purple) and target-subnetworks (green). Error bars indicate the standard error of the mean across all realizations and cross-validations. Red lines indicate significantly higher prediction accuracy than the baseline and chance level (binomial test, $P < 0.05$, FDR corrected for dependent samples).

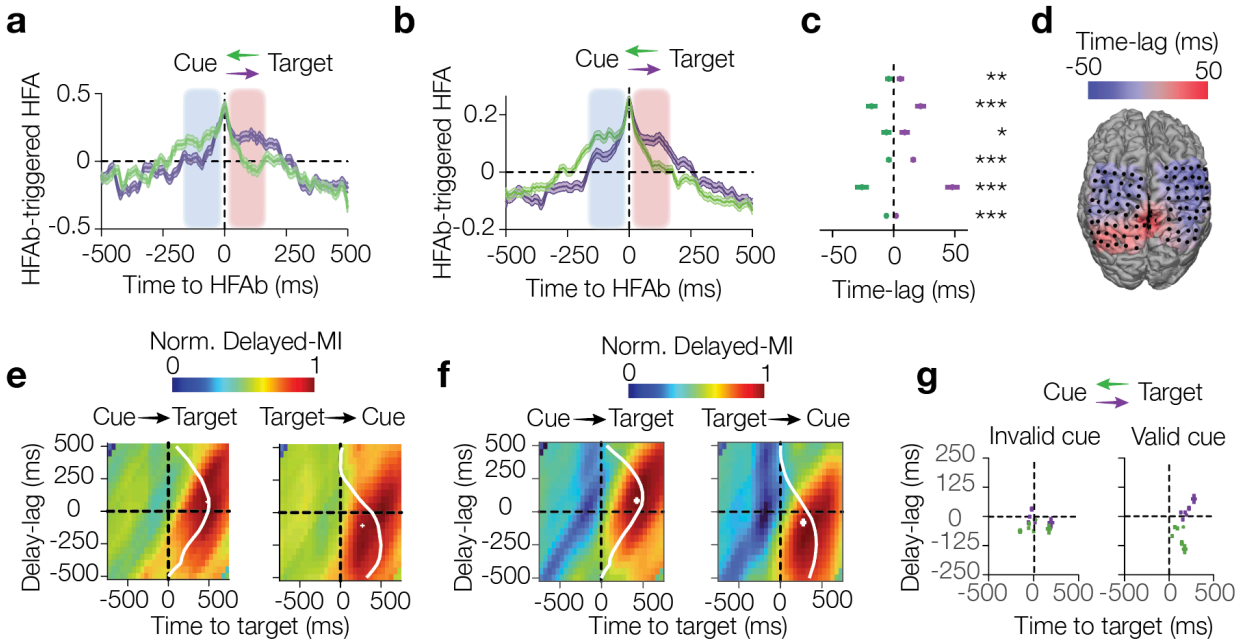

Fig. 4. Cue-subnetworks precede target-subnetworks during target processing. a, Example of HFAb-triggered HFA for HFAbs during target processing, when HFA is measured in target-subnetworks relative to HFAbs in cue-subnetworks (purple) vs HFA is measured in cue-subnetworks relative to HFAbs in target-subnetworks (green). Red and blue shades denote significant difference between directions denoting a cue lead and a target lag respectively (Wilcoxon rank-sum test, $P < 0.05$) **b,** Group-level average of HFAb-triggered HFA, similar to **a**. **c**, HFAb-triggered HFA median peak for electrode pairs corresponding to the same groups as in **b** (the Wilcoxon test was used to determine whether there was a difference in the distribution of peak positions between the two directions. Each row indicates the results for one individual. Error bars represent the standard error of the mean). **d**, An individual visualization example of the lead-lag patterns between electrodes in cue and target-subnetworks (across all cluster numbers) during the target processing period. The lead and lag temporal patterns are shown in a color gradient from red to blue. **e**, Heatmaps of normalized DMI values averaged across all members of the cue and target-subnetworks. The left panel shows DMI when the target-subnetwork is fixed, and the cue-subnetwork is shifted. The right panel shows DMI when the cue-subnetwork is fixed, and the target-subnetwork is shifted. The white line indicates the time-lag distribution of DMI peaks across electrode pairs. The cross signs indicate the median of DMI peak time-lags ± standard error. **f**, Group average of DMI across all individuals, similar to **e**. **g**, Comparisons of DMI peak distributions between the two opposite directions (green for shifting the cue-subnetwork and purple for shifting the target-subnetwork) for trials with valid (right) and invalid cues (left). Each individual is shown by a cross sign, which refers to the median ± standard error for DMI peaks across all electrode pairs between the two subnetworks.

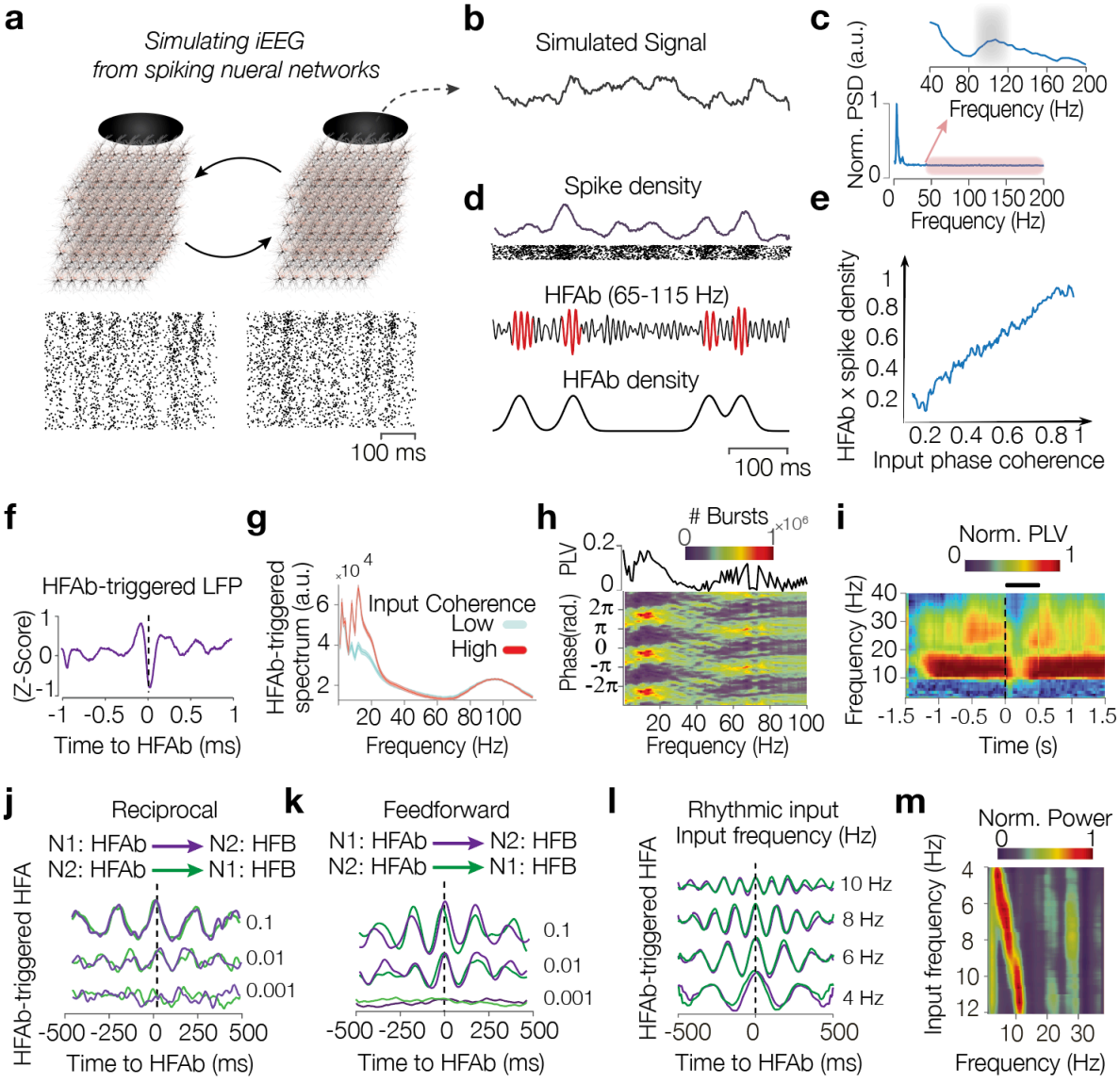

Fig. 5. Computational modeling of iEEG signals. a, Two interconnected cubic networks of point source spiking neurons were simulated (bottom panels show raster plots for neurons in each network). A recording disk was implemented on top of each network to measure neural activity. **b**, Example of simulated iEEG signals. **c**, The power spectral density (PSD) of iEEG signals. **d**, A single trial example of spike density and raster (top) detected HFAbs (middle, HFAbs are shown in red), and HFAb density (bottom). **e**, HFAb density and spike density show linearly increasing correlations as input coherence increases. **f**, HFAb-triggered LFP. **g**, Cycle-balanced power spectrum triggered around HFAbs when the input to the network has high (red) or low coherence (cyan). **h**, HFAb phase distribution at different frequencies. **i**, The PLV of HFAbs to low frequencies after a transient input (thick black line) is fed to the network. (**j, k**) HFAb-triggered HFA between (**j**) reciprocally connected and (**k**) directional feedforward networks (connections from N1 to N2, see **Extended Data Fig. 12e** for further details) with varying connectivity strengths (purple and green traces show HFAb-triggered HFA when bursts are extracted from N1 and N2, respectively). **l**, HFAb-triggered HFA between disconnected networks with shared rhythmic inputs. **m**, PSD over the HFAb-triggered HFA for rhythmic inputs of varying frequencies.

References

1. Saalmann, Y. B., Pigarev, I. N. & Vidyasagar, T. R. Neural Mechanisms of Visual Attention: How Top-Down Feedback Highlights Relevant Locations. *Science* **316**, 1612–1615 (2007).
2. Fries, P. Neuronal Gamma-Band Synchronization as a Fundamental Process in Cortical Computation. *Annual Review of Neuroscience* **32**, 209–224 (2009).
3. Gregoriou, G. G., Gotts, S. J., Zhou, H. & Desimone, R. High-Frequency, Long-Range Coupling Between Prefrontal and Visual Cortex During Attention. *Science* **324**, 1207–1210 (2009).
4. Szczepanski, S. M. *et al.* Dynamic Changes in Phase-Amplitude Coupling Facilitate Spatial Attention Control in Fronto-Parietal Cortex. *PLOS Biology* **12**, e1001936 (2014).
5. Buschman, T. J. & Kastner, S. From Behavior to Neural Dynamics: An Integrated Theory of Attention. *Neuron* **88**, 127–144 (2015).
6. Fiebelkorn, I. C. & Kastner, S. Functional Specialization in the Attention Network. *Annu Rev Psychol* **71**, 221–249 (2020).
7. Banaie Boroujeni, K. & Womelsdorf, T. Routing states transition during oscillatory bursts and attentional selection. *Neuron* (2023) doi:10.1016/j.neuron.2023.06.012.
8. Womelsdorf, T. & Fries, P. Neuronal coherence during selective attentional processing and sensory–motor integration. *Journal of Physiology-Paris* **100**, 182–193 (2006).
9. Doesburg, S. M., Roggeveen, A. B., Kitajo, K. & Ward, L. M. Large-Scale Gamma-Band Phase Synchronization and Selective Attention. *Cerebral Cortex* **18**, 386–396 (2008).

10. Lakatos, P., Karmos, G., Mehta, A. D., Ulbert, I. & Schroeder, C. E. Entrainment of Neuronal Oscillations as a Mechanism of Attentional Selection. *Science* **320**, 110–113 (2008).

11. Siegel, M., Donner, T. H., Oostenveld, R., Fries, P. & Engel, A. K. Neuronal Synchronization along the Dorsal Visual Pathway Reflects the Focus of Spatial Attention. *Neuron* **60**, 709–719 (2008).

12. Hirvonen, J., Monto, S., Wang, S. H., Palva, J. M. & Palva, S. Dynamic large-scale network synchronization from perception to action. *Network Neuroscience* **2**, 442–463 (2018).

13. Buschman, T. J. & Miller, E. K. Top-Down Versus Bottom-Up Control of Attention in the Prefrontal and Posterior Parietal Cortices. *Science* **315**, 1860–1862 (2007).

14. Siegel, M., Buschman, T. J. & Miller, E. K. Cortical information flow during flexible sensorimotor decisions. *Science* **348**, 1352–1355 (2015).

15. Michalareas, G. *et al.* Alpha-Beta and Gamma Rhythms Subserve Feedback and Feedforward Influences among Human Visual Cortical Areas. *Neuron* **89**, 384–397 (2016).

16. Fan, J., McCandliss, B. D., Fossella, J., Flombaum, J. I. & Posner, M. I. The activation of attentional networks. *NeuroImage* **26**, 471–479 (2005).

17. Canolty, R. T. *et al.* Oscillatory phase coupling coordinates anatomically dispersed functional cell assemblies. *PNAS* **107**, 17356–17361 (2010).

18. Braun, U. *et al.* Dynamic reconfiguration of frontal brain networks during executive cognition in humans. *Proceedings of the National Academy of Sciences* **112**, 11678–11683 (2015).

19. Bassett, D. S. & Sporns, O. Network neuroscience. *Nat Neurosci* **20**, 353–364 (2017).

20. Avena-Koenigsberger, A., Misic, B. & Sporns, O. Communication dynamics in complex brain networks. *Nat Rev Neurosci* **19**, 17–33 (2018).

21. Brookes, M. J. *et al.* Measuring functional connectivity using MEG: Methodology and comparison with fcMRI. *NeuroImage* **56**, 1082–1104 (2011).

22. Hari, R. & Parkkonen, L. The brain timewise: how timing shapes and supports brain function. *Philosophical Transactions of the Royal Society B: Biological Sciences* **370**, 20140170 (2015).

23. Higley, M. J. & Cardin, J. A. Spatiotemporal dynamics in large-scale cortical networks. *Current Opinion in Neurobiology* **77**, 102627 (2022).

24. Lachaux, J.-P., Axmacher, N., Mormann, F., Halgren, E. & Crone, N. E. High-frequency neural activity and human cognition: past, present and possible future of intracranial EEG research. *Prog Neurobiol* **98**, 279–301 (2012).

25. Parvizi, J. & Kastner, S. Human Intracranial EEG: Promises and Limitations. *Nat Neurosci* **21**, 474–483 (2018).

26. Ray, S., Niebur, E., Hsiao, S. S., Sinai, A. & Crone, N. E. High-frequency gamma activity (80-150 Hz) is increased in human cortex during selective attention. *Clin Neurophysiol* **119**, 116–133 (2008).

27. Voytek, B. *et al.* Oscillatory dynamics coordinating human frontal networks in support of goal maintenance. *Nat Neurosci* **18**, 1318–1324 (2015).

28. Haller, M. *et al.* Persistent neuronal activity in human prefrontal cortex links perception and action. *Nat Hum Behav* **2**, 80–91 (2018).

29. Helfrich, R. F. *et al.* Neural Mechanisms of Sustained Attention Are Rhythmic. *Neuron* **99**, 854-865.e5 (2018).

30. Martin, A. B. *et al.* Temporal Dynamics and Response Modulation across the Human Visual System in a Spatial Attention Task: An ECoG Study. *J. Neurosci.* **39**, 333–352 (2019).

31. Jacques, C., Jonas, J., Colnat-Coulbois, S., Maillard, L. & Rossion, B. Low and high frequency intracranial neural signals match in the human associative cortex. *eLife* **11**, e76544 (2022).

32. Ray, S. & Maunsell, J. H. R. Different Origins of Gamma Rhythm and High-Gamma Activity in Macaque Visual Cortex. *PLOS Biology* **9**, e1000610 (2011).

33. Banaie Boroujeni, K., Tiesinga, P. & Womelsdorf, T. Adaptive spike-artifact removal from local field potentials uncovers prominent beta and gamma band neuronal synchronization. *Journal of Neuroscience Methods* **330**, 108485 (2020).

34. Leszczyński, M. *et al.* Dissociation of broadband high-frequency activity and neuronal firing in the neocortex. *Science Advances* **6**, eabb0977 (2020).

35. Leonard, M. K. *et al.* Large-scale single-neuron speech sound encoding across the depth of human cortex. *Nature* **626**, 593–602 (2024).

36. Zolnik, T. A. *et al.* Layer 6b controls brain state via apical dendrites and the higher-order thalamocortical system. *Neuron* **112**, 805-820.e4 (2024).

37. Canolty, R. T. & Knight, R. T. The functional role of cross-frequency coupling. *Trends in Cognitive Sciences* **14**, 506–515 (2010).

38. Arnulfo, G. *et al.* Long-range phase synchronization of high-frequency oscillations in human cortex. *Nat Commun* **11**, 5363 (2020).

39. Williams, N. *et al.* Modules in connectomes of phase-synchronization comprise anatomically contiguous, functionally related regions. *NeuroImage* **272**, 120036 (2023).

678 40. Garrett, J. C. *et al.* Binding of cortical functional modules by synchronous high-frequency
679 oscillations. *Nat Hum Behav* 1–15 (2024) doi:10.1038/s41562-024-01952-2.
680 41. Jensen, O. & Colgin, L. L. Cross-frequency coupling between neuronal oscillations. *Trends*
681 *in Cognitive Sciences* **11**, 267–269 (2007).
682 42. Jiang, H., Bahramisharif, A., van Gerven, M. A. J. & Jensen, O. Measuring directionality
683 between neuronal oscillations of different frequencies. *NeuroImage* **118**, 359–367 (2015).
684 43. Bonnefond, M., Kastner, S. & Jensen, O. Communication between Brain Areas Based on
685 Nested Oscillations. *eNeuro* **4**, ENEURO.0153-16.2017 (2017).
686 44. Kam, J. W. Y. *et al.* Default network and frontoparietal control network theta connectivity
687 supports internal attention. *Nat Hum Behav* **3**, 1263–1270 (2019).
688 45. Johnson, E. L. *et al.* A rapid theta network mechanism for flexible information encoding.
689 *Nat Commun* **14**, 2872 (2023).
690 46. Izhikevich, E. M. Which model to use for cortical spiking neurons? *IEEE Transactions on*
691 *Neural Networks* **15**, 1063–1070 (2004).
692 47. Colgin, L. L. *et al.* Frequency of gamma oscillations routes flow of information in the
693 hippocampus. *Nature* **462**, 353–357 (2009).
694 48. Akam, T. & Kullmann, D. M. Oscillations and Filtering Networks Support Flexible Routing
695 of Information. *Neuron* **67**, 308–320 (2010).
696 49. Yamamoto, J., Suh, J., Takeuchi, D. & Tonegawa, S. Successful Execution of Working
697 Memory Linked to Synchronized High-Frequency Gamma Oscillations. *Cell* **157**, 845–857
698 (2014).
699 50. Palmigiano, A., Geisel, T., Wolf, F. & Battaglia, D. Flexible information routing by
700 transient synchrony. *Nat Neurosci* **20**, 1014–1022 (2017).

51. Lundqvist, M., Herman, P., Warden, M. R., Brincat, S. L. & Miller, E. K. Gamma and beta bursts during working memory readout suggest roles in its volitional control. *Nat Commun* **9**, 394 (2018).

52. Hahn, G., Ponce-Alvarez, A., Deco, G., Aertsen, A. & Kumar, A. Portraits of communication in neuronal networks. *Nat Rev Neurosci* **20**, 117–127 (2019).

53. Fernandez-Ruiz, A., Sirota, A., Lopes-dos-Santos, V. & Dupret, D. Over and above frequency: Gamma oscillations as units of neural circuit operations. *Neuron* **111**, 936–953 (2023).

54. Bosman, C. A. *et al.* Attentional Stimulus Selection through Selective Synchronization between Monkey Visual Areas. *Neuron* **75**, 875–888 (2012).

55. Engel, T. A. *et al.* Selective modulation of cortical state during spatial attention. *Science* **354**, 1140–1144 (2016).

56. König, P., Engel, A. K. & Singer, W. Relation between oscillatory activity and long-range synchronization in cat visual cortex. *Proceedings of the National Academy of Sciences* **92**, 290–294 (1995).

57. Roelfsema, P. R., Engel, A. K., König, P. & Singer, W. Visuomotor integration is associated with zero time-lag synchronization among cortical areas. *Nature* **385**, 157–161 (1997).

58. Uhlhaas, P. J. *et al.* Neural Synchrony in Cortical Networks: History, Concept and Current Status. *Front Integr Neurosci* **3**, 17 (2009).

59. Gollo, L. L., Mirasso, C. & Villa, A. E. P. Dynamic control for synchronization of separated cortical areas through thalamic relay. *NeuroImage* **52**, 947–955 (2010).

60. Gollo, L. L., Mirasso, C. R., Atienza, M., Crespo-Garcia, M. & Cantero, J. L. Theta Band Zero-Lag Long-Range Cortical Synchronization via Hippocampal Dynamical Relaying. *PLOS ONE* **6**, e17756 (2011).

61. Saalmann, Y. B. & Kastner, S. Cognitive and Perceptual Functions of the Visual Thalamus. *Neuron* **71**, 209–223 (2011).

62. Logothetis, N. K. *et al.* Hippocampal–cortical interaction during periods of subcortical silence. *Nature* **491**, 547–553 (2012).

63. Sara, S. J. & Bouret, S. Orienting and Reorienting: The Locus Coeruleus Mediates Cognition through Arousal. *Neuron* **76**, 130–141 (2012).

64. Saalmann, Y. B., Pinsk, M. A., Wang, L., Li, X. & Kastner, S. The Pulvinar Regulates Information Transmission Between Cortical Areas Based on Attention Demands. *Science* (2012) doi:10.1126/science.1223082.

65. Vijayan, S. & Kopell, N. J. Thalamic model of awake alpha oscillations and implications for stimulus processing. *Proceedings of the National Academy of Sciences* **109**, 18553–18558 (2012).

66. Fiebelkorn, I. C., Pinsk, M. A. & Kastner, S. The mediodorsal pulvinar coordinates the macaque fronto-parietal network during rhythmic spatial attention. *Nat Commun* **10**, 215 (2019).

67. Kastner, S., Fiebelkorn, I. C. & Eradath, M. K. Dynamic pulvino-cortical interactions in the primate attention network. *Current Opinion in Neurobiology* **65**, 10–19 (2020).

68. Menara, T., Qin, Y., Bassett, D. S. & Pasqualetti, F. Relay Interactions Enable Remote Synchronization in Networks of Phase Oscillators. *IEEE Control Systems Letters* **6**, 500–505 (2022).

69. Gollo, L. L., Mirasso, C., Sporns, O. & Breakspear, M. Mechanisms of Zero-Lag Synchronization in Cortical Motifs. *PLOS Computational Biology* **10**, e1003548 (2014).

70. Zolnik, T. A. *et al.* Layer 6b Is Driven by Intracortical Long-Range Projection Neurons. *Cell Reports* **30**, 3492-3505.e5 (2020).

71. Fox, M. D. & Raichle, M. E. Spontaneous fluctuations in brain activity observed with functional magnetic resonance imaging. *Nat Rev Neurosci* **8**, 700–711 (2007).

72. Smith, S. M. *et al.* Correspondence of the brain's functional architecture during activation and rest. *Proceedings of the National Academy of Sciences* **106**, 13040–13045 (2009).

73. Srivastava, P. *et al.* Models of communication and control for brain networks: distinctions, convergence, and future outlook. *Netw Neurosci* **4**, 1122–1159 (2020).

74. Engel, T. A., Schölvinck, M. L. & Lewis, C. M. The diversity and specificity of functional connectivity across spatial and temporal scales. *NeuroImage* **245**, 118692 (2021).

75. Wang, X.-J. & Yang, G. R. A disinhibitory circuit motif and flexible information routing in the brain. *Current Opinion in Neurobiology* **49**, 75–83 (2018).

76. Battiston, F. *et al.* Networks beyond pairwise interactions: Structure and dynamics. *Physics Reports* **874**, 1–92 (2020).

77. Bressler, S. L. & Menon, V. Large-scale brain networks in cognition: emerging methods and principles. *Trends in Cognitive Sciences* **14**, 277–290 (2010).

78. Jensen, O., Gips, B., Bergmann, T. O. & Bonnefond, M. Temporal coding organized by coupled alpha and gamma oscillations prioritize visual processing. *Trends in Neurosciences* **37**, 357–369 (2014).

79. Chapeton, J. I., Haque, R., Wittig, J. H., Inati, S. K. & Zaghloul, K. A. Large-Scale Communication in the Human Brain Is Rhythmically Modulated through Alpha Coherence. *Current Biology* **29**, 2801-2811.e5 (2019).

80. Harris, K. D. & Thiele, A. Cortical state and attention. *Nat Rev Neurosci* **12**, 509–523 (2011).

81. Gast, R., Solla, S. A. & Kennedy, A. Neural heterogeneity controls computations in spiking neural networks. *Proceedings of the National Academy of Sciences* **121**, e2311885121 (2024).

82. Hanslmayr, S., Staudigl, T. & Fellner, M.-C. Oscillatory power decreases and long-term memory: the information via desynchronization hypothesis. *Front. Hum. Neurosci.* **6**, (2012).

83. Hanslmayr, S., Staresina, B. P. & Bowman, H. Oscillations and Episodic Memory: Addressing the Synchronization/Desynchronization Conundrum. *Trends in Neurosciences* **39**, 16–25 (2016).

84. Beaman, C. B., Eagleman, S. L. & Dragoi, V. Sensory coding accuracy and perceptual performance are improved during the desynchronized cortical state. *Nat Commun* **8**, 1308 (2017).

85. Nandy, A., Nassi, J. J., Jadi, M. P. & Reynolds, J. Optogenetically induced low-frequency correlations impair perception. *eLife* **8**, e35123 (2019).

86. Weisz, N., Kraft, N. G. & Demarchi, G. Auditory cortical alpha/beta desynchronization prioritizes the representation of memory items during a retention period. *eLife* **9**, e55508 (2020).

87. Egly, R., Driver, J. & Rafal, R. D. Shifting visual attention between objects and locations: Evidence from normal and parietal lesion subjects. *Journal of Experimental Psychology: General* **123**, 161–177 (1994).

88. Fiebelkorn, I. C., Saalmann, Y. B. & Kastner, S. Rhythmic Sampling within and between Objects despite Sustained Attention at a Cued Location. *Current Biology* **23**, 2553–2558 (2013).

89. Boashash, B. Estimating and Interpreting the Instantaneous Frequency of a Signal – Part 1: Fundamentals. in *Proceedings of the Ieee* 520–538 (1992).

90. Hill, M. R. H., Fried, I. & Koch, C. Quantification and classification of neuronal responses in kernel-smoothed peristimulus time histograms. *Journal of Neurophysiology* **113**, 1260–1274 (2015).

91. Dunn, O. J. Multiple Comparisons among Means. *Journal of the American Statistical Association* **56**, 52–64 (1961).

92. Benjamini, Y. & Yekutieli, D. False Discovery Rate–Adjusted Multiple Confidence Intervals for Selected Parameters. *Journal of the American Statistical Association* **100**, 71–81 (2005).

93. Fisher, N. I. *Statistical Analysis of Circular Data*. (Cambridge University Press, 1995).

94. Milligan, G. W. & Cooper, M. C. An examination of procedures for determining the number of clusters in a data set. *Psychometrika* **50**, 159–179 (1985).

95. Jain, A. K. & Dubes, R. C. *Algorithms for Clustering Data*. (Prentice-Hall, Inc., USA, 1988).

96. Halkidi, M., Batistakis, Y. & Vazirgiannis, M. On Clustering Validation Techniques. *Journal of Intelligent Information Systems* **17**, 107–145 (2001).

812 97. Vendramin, L., Campello, R. J. G. B. & Hruschka, E. R. Relative clustering validity
813 criteria: A comparative overview. *Statistical Analysis and Data Mining: The ASA Data*
814 *Science Journal* **3**, 209–235 (2010).
815 98. Freedman, D. & Diaconis, P. On the histogram as a density estimator:L2 theory. *Z.*
816 *Wahrscheinlichkeitstheorie verw Gebiete* **57**, 453–476 (1981).
817 99. Billeh, Y. N. *et al.* Systematic Integration of Structural and Functional Data into Multi-scale
818 Models of Mouse Primary Visual Cortex. *Neuron* **106**, 388-403.e18 (2020).
819 100. Potjans, T. C. & Diesmann, M. The Cell-Type Specific Cortical Microcircuit: Relating
820 Structure and Activity in a Full-Scale Spiking Network Model. *Cerebral Cortex* **24**, 785–
821 806 (2014).
822 101. Barral, J. & D Reyes, A. Synaptic scaling rule preserves excitatory–inhibitory balance and
823 salient neuronal network dynamics. *Nat Neurosci* **19**, 1690–1696 (2016).
824 102. Izhikevich, E. M. Simple model of spiking neurons. *IEEE Transactions on Neural*
825 *Networks* **14**, 1569–1572 (2003).
826 103. Pfeffer, C. K., Xue, M., He, M., Huang, Z. J. & Scanziani, M. Inhibition of inhibition in
827 visual cortex: the logic of connections between molecularly distinct interneurons. *Nat*
828 *Neurosci* **16**, 1068–1076 (2013).
829 104. Karnani, M. M. *et al.* Cooperative Subnetworks of Molecularly Similar Interneurons in
830 Mouse Neocortex. *Neuron* **90**, 86–100 (2016).
831 105. Medalla, M., Gilman, J. P., Wang, J.-Y. & Luebke, J. I. Strength and Diversity of Inhibitory
832 Signaling Differentiates Primate Anterior Cingulate from Lateral Prefrontal Cortex. *J.*
833 *Neurosci.* **37**, 4717–4734 (2017).

834 106. Gilman, J. P., Medalla, M. & Luebke, J. I. Area-Specific Features of Pyramidal Neurons—a
835 Comparative Study in Mouse and Rhesus Monkey. *Cerebral Cortex* **27**, 2078–2094 (2017).
836 107. Medalla, M. & Luebke, J. I. Diversity of Glutamatergic Synaptic Strength in Lateral
837 Prefrontal versus Primary Visual Cortices in the Rhesus Monkey. *J. Neurosci.* **35**, 112–127
838 (2015).
839 108. Amatrudo, J. M. *et al.* Influence of Highly Distinctive Structural Properties on the
840 Excitability of Pyramidal Neurons in Monkey Visual and Prefrontal Cortices. *J. Neurosci.*
841 **32**, 13644–13660 (2012).
842 109. Roxin, A., Brunel, N., Hansel, D., Mongillo, G. & Vreeswijk, C. van. On the Distribution of
843 Firing Rates in Networks of Cortical Neurons. *J. Neurosci.* **31**, 16217–16226 (2011).
844 110. Milstein, J., Mormann, F., Fried, I. & Koch, C. Neuronal Shot Noise and Brownian 1/f2
845 Behavior in the Local Field Potential. *PLOS ONE* **4**, e4338 (2009).
846 111. Bédard, C., Kröger, H. & Destexhe, A. Modeling Extracellular Field Potentials and the
847 Frequency-Filtering Properties of Extracellular Space. *Biophysical Journal* **86**, 1829–1842
848 (2004).
849
850

851 **Supplementary Materials**
852
853 **Methods**
854 **Extended Data Figs.** 1 to 12
855 **Supplementary** Tables 1 to 4
856

857 **Methods**

858 **Experimental model and subject details**

859 **Participants**. Intracranial recordings were obtained from 12 epilepsy patients who underwent pre-
860 surgical monitoring with implanted grid electrodes. Study 1 included seven patients (35.99 ± 12.42
861 years; mean ± SD; 5 females; see Helfrich et al., 2018 for further details). Patients were recruited
862 from the University of California, Irvine Medical Center, USA (n = 6) and California Pacific
863 Medical Center (CPMC), San Francisco, USA (n = 1). Study 2 included 5 patients (30.20 ± 1186
864 years; mean ± SD; 1 female, 3 patients were excluded from the original study due to their limited
865 electrode coverages; see Szczepanski et al., 2014 for further details) from Johns Hopkins Hospital
866 in Baltimore, MD, USA (N = 1) and Stanford Hospital, CA, USA (N = 4). The electrode placement
867 was entirely guided by clinical considerations, and all patients provided written informed consent
868 to participate in the study. All procedures were approved by the Institutional Review Board at each
869 site, as well as the Committee for Protection of Human Subjects at the University of California,
870 Berkeley (Protocol number: 2010-02-783) and were in accordance with the Declaration of
871 Helsinki.

872

873 **METHOD DETAILS**

874 **Experimental design and procedure**

875 **Behavioral tasks**. Participants performed a spatial attention task in each experiment. In
876 experiment 1, participants performed a variant of the Egly-Driver task (Egly et al., 1994;
877 Fiebelkorn et al., 2013; see Helfrich et al., 2018 for further details) Behavioral data were collected
878 with Presentation Software (Neurobehavioral Systems). Subjects were seated approximately 60
879 cm from the laptop screen. Subjects started each trial by pressing a left mouse button. On each

trial, after appearance of a fixation cross, two bars appeared vertically or horizontally on the screen, followed by a brief spatial cue (100 ms), presented after 400-800 ms at one of the four corners of the bar stimuli. The spatial cue indicated the location where the target was most likely to appear (72% cue validity) and occurred pseudo-randomly in any of the four quadrants. A variable cue-to-target interval (500 – 1700 ms) was introduced after the cue during which participants sustained spatial attention at the cued location. Targets could randomly appear at any point during the cue-target interval,and participants released the mouse button to report a detected target. Infrequent catch trials (10%) during which no actual target appeared were used to track the false alarm rate. Auditory feedback indicated whether the trial was performed correctly. The target luminance was adjusted every 15 trials, if necessary, by increasing/decreasing the RGB value, in order to achieve an overall approximate accuracy of 80%. The experimenter monitored continuous fixation. All participants responded by using the hand contralateral to the implanted grid, except for participant S5 who had bilateral grids and responded by using the left hand. Participants performed up to 5 blocks of 60 trials each (190 trials ± 67; mean ± SD).

Experiment 2 (Extended Data Fig. 1) used EPrime software (Psychology Software Tools) to control stimulus presentation (see Szczepanski et al., 2014 for more details). Subjects were seated approximately 60 cm away from the laptop screen. Each trial began with red circles (distractors) dynamically switching on and off on a dark background. A spatial cue guided participants to the right or left hemifield, and the cue remained on the screen throughout the trial. Subjects were instructed to maintain fixation and only covertly shift their attention to the cued hemifield. Through the trial, the experimenter monitored eye movements and ensured central fixation. After a variable cue-target interval (1000 – 2000 ms), a blue square target appeared on the screen (~62/38% on the cued/uncued hemifields). The target remained on the screen until the subject responded or the trial

903 ended (2000 ms timed out). Subjects were asked to report a target seen in a cued hemifield by
904 pressing a a button while withholding a response if the target was seen in a non-cued hemifield.
905 Targets appeared randomly during the cue-target interval. Three out of five subjects responded
906 with the hand ipsilateral to the grid. Each participant completed six blocks (each 42 trials). The
907 experimenter monitored eye movements and ensured central fixation throughout both experiments.
908
909 **ECoG data acquisition.** Electrophysiological and peripheral (photodiode) data were collected
910 using a Nihon Kohden recording system at UC Irvine, CPMC and Children's Hospital (128/256
911 channel, 1000/5000 Hz sampling rate), a Tucker Davis Technologies recording system at Stanford
912 (128 channel, 3052 Hz sampling rate), or a Natus Medical Stellate Harmonie recording system at
913 Johns Hopkins (128 channel, 1000 Hz sampling rate).
914
915 **Electrode localization**. In experiment 1, the electrodes were localized by transforming both the
916 pre-implant MRI and the post-implant computed tomography CT into Talairach space. For all
917 subjects, MNI coordinates were also calculated for each electrode location, which was used for
918 group-level visualizations (see Helfrich et al., 2018).In experiment 2, post-implant CT was aligned
919 to the pre-implant MRI and all were transformed into MNI space across subjects (see Szczepanski
920 et al., 2014). Strip or grid electrodes were implanted with 1 cm spacing. One participant (S5) had
921 an additional 8 contact depth probe inserted into the occipital cortex. Electrode positions were
922 primarily determined using the VTPM atlas (Wang et al., 2015). For electrodes without an assigned
923 label, the process was repeated using the AFNI atlas (Lancaster et al., 1997). The assigned
924 positions were manually verified and adjusted based on electrode reconstructions visualized in
925 native Talairach space. Electrodes near the Temporoparietal Junction (TPJ) were manually

926 localized, as TPJ definitions were not available in either the VTPM or AFNI atlases (see Helfrich
927 et al., 2018 for more details).
928
929 **iEEG Data**. Preprocessing: All intracranial EEG channels were manually examined by a
930 neurologist for epileptiform activity and artifacts. Affected channels and epochs were excluded.
931 The raw data was preprocessed using the EEGLAB and Fieldtrip toolbox in MATLAB.
932 Preprocessing included notch filtering at 60 Hz and all harmonics, as well as referencing the data
933 to the common mean of electrodes as previously described [4,29]. Then, the data was time locked to
934 individual trials. Trials were 8 seconds long, -3 to +5 seconds around cue onsets in the experiment
935 1 and -2 to +6 seconds around cue onsets in the experiment 2. As a control, we re-referenced the
936 datasets from common average referencing to local composite referencing (LCR), a spatial
937 Laplacian estimate relative to nearest neighbors. This re-referencing did not alter the main results.
938
939 **Analysis of high frequency activity bursts (HFAbs)**
940 **HFAb detection and density analysis.** We adopted an adaptive burst detection approach, similar
941 to previous work [7], to identify high-frequency oscillatory bursts (65-115 Hz) at each electrode.
942 The frequency band was selected based on spectral peaks observed across all individuals (87 Hz
943 trials ± 14; mean ± SD) and in the modeling. Similar analyses were conducted for a broader band
944 (65-175 Hz) and the low gamma band (35-65 Hz). While the broader band produced similar results,
945 the low gamma band yielded inconsistent responses and noisy clustering. We selected the
946 frequency band based on spectral peaks across individuals and in the modeling. First, we applied
947 a zero-phase Butterworth bandpass filter to the padded signal and then calculated the analytic

signal x(t) using the Hilbert transform. We extracted the instantaneous amplitude as the real part of the analytic signal $z(t)$ following eq. 1:

$$z(t) = x(t) + iy(t) = a(t)e^{i\theta(t)} \quad \text{eq. 1}$$

where $y(t)$ is the Hilbert transform of $x(t)$:

$$y(t) = \frac{1}{\pi} \int_{-\infty}^{+\infty} \frac{x(\tau)}{t-\tau}\, d\tau. \quad \text{eq. 2}$$

The instantaneous energy [89] $IE(t)$ of the signal is calculated from its Hilbert transform:

$$IE(t) = \int_0^{\omega_N} H^2(t,\omega)\, d\omega \quad \text{eq. 3}$$

$$\omega(t) = \frac{d\theta(t)}{dt} \quad \text{eq. 4}$$

where $\omega(t)$ corresponds to instantaneous angular velocity. If the frequency band is narrow and if the instantaneous frequency (eq. 4) is small enough, it can be approximated by squared $a(t)$, which is the instantaneous amplitude. The marginal mean energy of the signal then can be estimated as eq. 5:

$$\overline{IE} = \frac{1}{T} \int_0^T a(t)^2\, dt \quad \text{eq. 5}$$

where T represents the duration of the signal. For skewed energy distributions in empirical data, we determined a threshold by setting it to 3.3 times the standard deviation of a half-normal distribution based on the median energy, plus the mean energy.

To qualify as a burst, the energy level had to exceed this threshold for at least 1.5 cycles of the upper bond frequency, and the instantaneous amplitude needed to surpass $\sqrt{2}$ times the RMS of the peaks. Burst boundaries were marked by the closest points to a burst peak where either the instantaneous energy fell below the signal's mean energy or the deviation in instantaneous frequency exceeded the mean change plus two standard deviations. This was to exclude multi-component or noisy events. Bursts were considered significant if their duration was at least 2.5

970 times the upper bond frequency cycle and exceeded the average span of adjacent local minima of
971 the energy function. Finally, when bursts were too close (less than five frequency cycles apart),
972 only the burst with the higher energy peak was kept.
973 To estimate how HFAb events are distributed over time, we calculate the HFAb density by
974 convolving a vector of burst events with a gaussian window of 500 ms and a standard deviation of
975 100ms. After estimating the HFAb density for each channel and trial, we investigated whether the
976 cue and target stimuli affected burst density. For each electrode, the average burst density aligned
977 to the cue and target onsets were calculated separately. Following that, we normalized timeseries
978 to the baseline (1000 ms before each event onset) by subtracting the mean and dividing it by the
979 standard deviation (see **Fig. 1c**). This is a similar approach to the peri-stimulus time histogram
980 (PSTH) for spike trains [90].
981
982 **Visualization of individual and group average responses on 3D brains.** To visualize how HFAb
983 responses were topographically organized in the 3D brains, we plotted both individual (**Extended**
984 **Data Fig. 1e, 2c**) and group responses to cue (**Fig. 1f**) and target onset (**Fig. 1g**). Each electrode
985 value was calculated as the mean of Z-scores within 500 ms of cue and target onset. For individual
986 subjects, the plotted value for each electrode was linearly attenuated with distance from the
987 electrode and for a sphere of 1 cm radius (illustrating correct versus incorrect trials separately, **Fig.**
988 **1h**, **Extended Data Fig. 1e,2c**). The group average plot (**Fig. 1f,g, Extended Data Fig. 2b**) was
989 calculated using electrode locations from both experiments to better cover the entire brain. The
990 MNI coordinates of electrodes were used for rendering on a template brain (subject S4 from
991 experiment 1 and subject S12 from experiment 2 were excluded due to suboptimal wrapping of
992 Tal to MNI spaces). We set the value of all mesh surfaces to zero for each subject. Then, similar

993 to the plotting for individual data, we calculated the value for mesh surfaces by using linear
994 attenuation (the sphere radius was set to 2.5 cm in order to achieve a smoother visualization of the
995 whole brain). As a last step, we averaged the surface values across all subjects to find consistent
996 patterns of activations for the cue and target. We plotted the data onto 3D brain for correct and
997 incorrect trials separately.
998
999 **Statistical analysis of HFAb responses to cues and targets events.** After calculating the burst
1000 density and finding PSTH for each channel, we examined whether the HFAb responses evoked by
1001 cues (within a window of 500 ms after cue onset) and targets (750 ms after target) were
1002 significantly different from baseline. This analysis was done at the network level. The average
1003 responses of electrodes within the defined time window were determined using the normalized
1004 HFAb density for each channel. Wilcoxon signed-rank tests were then used to examine if there
1005 was a non-zero response at the network level to cue and target onsets. Also, we performed a linear
1006 regression analysis of the cue and target responses in electrodes under the null hypothesis that the
1007 cue and target responses are independent (**Fig. 1e**).
1008 To test whether cue and target responses were different when grouped by trial outcomes, we used
1009 the Kruskial Wallis test under the null hypothesis that cue, and target responses do not differ by
1010 outcome condition. For pairwise comparisons between different groups, we used Dunn's test [91]
1011 with Tukey-Kramer multiple comparison correction (**Fig. 1d**).
1012 We also tested whether and when burst density profiles in correct trials were different compared
1013 with other outcome conditions. We used the mean of HFAb-density in correct trials as a test
1014 statistic. We then randomly selected 1000 samples by permuting trial outcome labels and for each
1015 randomly selected sample computed the 95% confidence intervals (CIs) around the mean. For

multiple comparison correction, we repeated the random permutation 1000 times and constructed 95% CIs on all 1000 CIs of randomly selected samples under the null hypothesis that the HFAb-density for correct trials was not different from randomly labeled trials at any timepoint relative to cue and target onsets separately (**Extended Data Fig. 2a**).

Identifying cue-responsive electrodes. We identified Cue+/- electrodes by determining increased HFAb rate or density profile within window of 500 ms after cue onsets. For each electrode, we compared the average HFAb density following cue onset with that at baseline using Wilcoxon rank-sum test. Electrodes with significant increases in HFAb rate after cue onset were labeled as Cue+ electrodes, while the remaining electrodes were labeled as Cue- electrodes, which was subsequently used in the classification (**Fig. 1k**).

Generalized Linear Mixed Effect Models. We used generalized linear mixed effects (GLMEs) models to examine the effects of each task variable on HFAb response to cue and target events. Three main predictors were used for the independent variables: *Laterality* (if the cue was either ipsilateral or contralateral to the electrode) with two levels (*Ipsi* and *Contra*), *Validity* (if the target appeared at the cued location) with two levels (*valid* and *invalid*), and trial outcome with four levels (*Correct hit, False alarm, Correct Rejection, Miss*). Since not all subjects had trials for all four outcome conditions, an alternative analysis also considered outcome as a binary variable (*Correct* and *Incorrect*) with a logit link function. The random effect was determined by considering groups as subject and channel labels. The response variable was either the mean burst density in response to the target or the cue. The GLME is then formalized as shown in eq. 6:

$$Response_{cue/target} = Laterality + Validity + Outcome + (1|Subject) + (1|Channel) + b + \varepsilon \quad \text{eq. 6}$$

Training classifiers for predicting trial outcome based on HFAb density around cue onset. A time-resolved classification approach was used to determine how accurately HFAb responses evoked by sensory cues could predict trial outcomes. First, we selected electrodes that showed a significant HFAb responses to the cue presentation (*Cue+* electrodes, see above), for which we then calculated the average HFAb density for *Cue+* electrodes for each trial and subject. Next, we tested whether the average burst density in sliding windows around the cue onset could predict the outcome at the trial level with a sliding window of 350 ms and a step of 25 ms. We used binary Support Vector Machine (SVM) with one-to-one comparisons of HFAb density in sliding windows with five folds of cross-validation. For training each SVM, a vector of the HFAb density in each sliding window was used along with a vector of outcome labels (*"Correct"* = 1, *"Incorrect"* = 0). The classifier used a Gaussian radial basis function kernel with a scaling factor of one. We assured that the number of correct and incorrect trials used in the training was identical, to prevent sample size biases. As the number of incorrect trials were lower than the number of correct trials, we randomly sampled correct trials with a sampling size equal to the number of incorrect trials in each fold. For each sliding window, we trained the classifier 1000 times and calculated the average accuracy and confusion matrix across all iterations and folds. (**Fig. 1k).**

To determine whether HFAb density after cue onset could more accurately predict trial outcome than chance and baseline, we used a binomial test on the accuracy of each window against the maximum value of baseline and chance-level prediction accuracy. After obtaining a p-value for each binomial test, we corrected the p-values using false discovery rate (FDR) for dependent

samples with a 0.05 alpha level [92] to correct for multiple comparisons error rate across all windows. We performed this procedure separately for each experiment (**Fig. 1k, Extended Data Fig. 3h**). In our main analysis, we pooled data across all subjects in each experiment due to the low number of trials per subject. However, to ensure that the results were not solely dependent on one subject, we ran a control analysis in which one subject was left out each time and the classifier was trained and tested. Controlled analyses in both experiments demonstrated that our observation was not based solely on one subject (**Extended Data Fig. 3i**). We used a similar approach for training the classifier on cue and target-subnetworks to train the classifier on cue and target-subnetworks, as further detailed in the 'Identifying synchronous subnetworks' section.

HFAb-triggered LFP analysis

We asked whether HFAbs on average were systematically related to any evoked potentials at lower frequencies. To address this question, we extracted a segment of 2 seconds around each burst (1 second before and after) and calculated the average HFAb-triggered potential for each electrode. The HFAb-triggered LFP was then averaged across all electrodes in each subject (**Fig. 2a**). A similar analysis was performed on the simulation results, but with a duration window of one second around HFAbs due to shorter trial lengths in simulations (**Fig. 5f**).

HFAb-triggered spectrum and Phase Locking Value (PLV) analysis. To understand the spectral dynamics of HFAbs and local population activities, we performed HFAb-triggered spectrum analyses using HFAb centers as discrete points. We estimated the PLV of points (burst centers) to their local field activity dynamics (both in the modeling and electrophysiological data) in order to investigate the phase synchronization of HFAbs within their local networks. We

calculated the HFAb-triggered spectrum using an adaptive window around HFAbs. We extracted a window centered around each selected point (HFAb center), which covered 2.5 cycles of the frequency of interest before and after the selected point. This window was then multiplied by a Hanning window. We estimated the power spectrum for each window using the Fast Fourier Transform (FFT) for frequencies ranging from 1 Hz to 100 Hz. To account for trial-wise power variations, triggered spectrum estimates were normalized by dividing by total power. We averaged spectrum estimates across all points and trials to calculate the final HFAb-triggered spectrum.

Following the analysis of the HFAb-triggered spectrum, a PLV calculation was performed to quantify the level of phase consistency of the HFAbs across trials for the frequencies of interest. The phase angle for each frequency was calculated based on the FFT results from the HFAb-triggered spectrum analysis. The PLV of HFAbs at each frequency was then calculated as the mean resultant in eq. 7:

$$\mathrm{PLV(f)} = \left|\frac{1}{N}\sum_{n=1}^{N} e^{i\phi_{f,n}}\right| \qquad \text{eq. 7}$$

where N is the total number of HFAbs and $\phi_{f,n}$ denotes the phase angle for the n^{th} HFAb at frequency *f*. The statistical significance of the observed PLV values was determined using a non-parametric permutation test with 1000 permutations and the Rayleigh test corrected for multiple comparisons, at 0.05. Peaks that passed both tests and had a prominence of 25% higher than the PLV range were considered significant (shown in black dots in **Fig. 2c**).

Time-resolved PLV analysis. To quantify the temporal dynamics of the phase synchronization of HFAbs with the low frequency LFP during cue and target processing, we extracted the phase of HFAbs at each frequency as explained above. Then, we used a sliding window of 500 ms with a step of 25 ms between -1500 and 1500 ms around the cue and target onsets separately. PLV was

calculated for each sliding window and across all trials (different types of trials were analyzed separately, e.g., correct trials and incorrect trials). We set a minimum number of data points of 50 bursts for the analysis (to achieve reliable statistics on circular data, Fisher, 1995). We measured the PLV for 1000 samples of 25 HFAbs drawn randomly from a population of HFAbs in each time bin to control for the number of bursts. The PLV for each time bin was calculated as the average PLV across all randomly drawn samples. The average PLV value for each subject and for all subjects in each experiment was calculated separately.

To test whether HFAb phase synchronization differed during cue and target processing, we used a channel-specific randomization test. For each recording channel and time bin, 1000 subsamples of HFAbs were randomly selected from the baseline period (within 1 second before each event). For each channel, each time bin, and each frequency, we calculated the upper and lower bond CIs (2.5% most extreme PLVs). For multiple comparison correction, we repeated this procedure 1000 time and found the most extreme 2.5% value across all CIs for time bins under the null hypothesis that the PLV for each time bin and frequency is not significantly different from the baseline value. Each time-frequency bin was considered significant if it differed from the critical values (**Extended Data Fig. 4d**). Each electrode and frequency band (theta/alpha (4-14 Hz) and beta (15-25 Hz)) for a time bin was considered significant if it showed a significantly different PLV from the baseline in more than 25% of the frequency points in that frequency band. Next, we computed the mean number of electrodes with significantly different PLVs than the randomized PLV distribution for each subject. Using the binomial test, we determined whether the proportion of electrodes with significantly lower PLV after the cue and target onset was different from the baseline level as well as the chance level (5%, **Fig. 2e**). To adjust for multiple comparisons, we used FDR for dependent samples and an alpha level of 0.05.

We also performed a control analysis to ensure that event-evoked iEEG signals are not confounding the variation in synchronization. First, we extracted -1.5 to 1.5 seconds around cue- and target-aligned iEEG signals for each electrode and trial. We averaged the data across all trials and removed the average event-triggered iEEG signal from individual trials. The same synchronization and statistical analyses were then performed on the trial with event-evoked iEEG subtracted. Subtraction of event-evoked iEEG did not change the main results pattern (**Extended Data Fig. 4e**).

Analysis of Coupling ratio. A Coupling Ratio (CR) index was defined to compare PLV after cue and target events as compared to baseline. We used this CR index also to visualize coupling variation in both 3D brain renderings (**Fig. 2f**), and the average network level coupling analysis (**Fig. 2h,i**). We calculated the coupling ratio by:

$$CR = \frac{PLV_{event} - PLV_{baseline}}{PLV_{baseline}} \quad \text{eq. 8}$$

Where the $PLV_{baseline}$ is the average PLV for each electrode within 1 second before the event, and PLV_{event} is the average PLV for each electrode within 0.5 seconds after the event. In this context, network decoupling is defined as a negative CR value indicating a reduction in PLV relative to the baseline. We show the CR value at both cue and target events for each subject.

We also used GLME models to investigate the effect of cue and target response on the coupling ratio following cue and target onsets (**Fig. 2h,i**). The GLME is formalized as shown in eq. 9:

$$Coupling\ Ratio_{cue/target} = Response_{cue} + Response_{target} + (1|Subject) + b + \varepsilon \quad \text{eq. 9}$$

<u>Quantification and Spectral analysis of HFAb-triggered HFA</u>

We calculated the interaction between HFAbs and HFA between each pair of electrodes. To estimate HFA, first we used a zero-phase Butterworth filter with cut-off frequencies of 65 Hz and 175 Hz to bandpass filter the signal. We chose the HFA frequency band broader to capture larger spectral content (similar results were obtained by choosing 65-115 Hz band). Next, we performed a Hilbert transform and used the real part of the analytical signal as HFA amplitude (eq. 1). We extracted a duration of one second around each HFAb from the HFA signal. We then calculated the HFAb-triggered HFA for each individual burst event as well as the average value for all bursts between each pair of electrodes. Our main analyses were restricted to HFAb-triggered HFA that occurred outside of the main behavioral epochs; either before cues or after target detection (for those without a response 1 second following target presentation). To control for any burst-independent correlations of iEEG signals across electrodes, we first calculated the HFAb-triggered HFA using randomly assigned burst times. Each burst was jittered with a random time lag of ±1000 ms. We then subtracted this jittered HFAb-triggered HFA from the original for further analysis. We calculated the spectral power of HFAb-triggered HFA across all electrode pairs to assess how HFA is organized relative to HFAbs recorded on other channels. The power spectral density was computed over the ±500 ms time window using a hanning taper. Additionally, we analyzed peak prominence for all pairs and plotted the distribution of spectral peaks. For each pair of electrodes, we extracted the prominent spectral peaks and plotted their distribution.

Dimensionality reduction of high-frequency coordination patterns. To identify prominent patterns of high-frequency activity coordination within the brain network, we analyzed a high-dimensional space of HFAb-triggered HFA across all electrode pairs for each subject, with each

electrode pair representing a single dimension. Using the HFAb-triggered HFA population, we calculated the covariance matrix C by:

$$C = \frac{1}{n-1}\sum_{i=1}^{n}(X_i - \bar{X})(X_i - \bar{X})^T \quad \text{eq. 10}$$

where X_i shows each HFAb-triggered HFA time series, n is the total number of electrode pairs, $\bar{X}$ is the marginal mean, and X^T is the transpose matrix of X. We found the eigenvectors of C as in eq. 11:

$$C = VDV^T \quad \text{eq. 11}$$

where V columns are the eigenvectors and principal components (PCs), and D contains eigenvalues indicating how much variance each component explains. In all participants, PC1 showed a near-symmetric activity state and explained more than 10% of variance in HFAb-triggered HFA dynamics over the population of electrode pairs (we used multistep Wilcoxon rank-sum test to examine if there was asymmetry of HFA within mirrored time windows around the HFAbs). By projecting the original data to the PC vector space, we calculated the HFAb-triggered HFA scores as:

$$Score = XC \quad \text{eq. 12}$$

We then used the scores of electrode pairs on the first component as their loading values on the synchronous component of the population.

Identifying synchronous subnetworks. Based on the scores of each electrode pair on the synchronous principal component, we generated a network synchrony matrix that describes synchronous inter-electrode interactions. For each electrode, we then defined a vector of variables with a dimension equal to the total number of electrodes. Each element of this vector describes the score of an electrode pair on the synchronous component. This vector was defined for all

electrodes, which generated a matrix in which each row represented one observation (electrode) and each column represented the score of the observed electrode on another electrode.

$$S_i = Score\ (X_{i,\ 1:n}) \qquad \text{eq. 13}$$

Using this matrix, we clustered the electrodes using resampling-based consensus K-Means algorithm with a correlational defined distance as in eq. 14:

$$d_{i,j} = 1 - r(S_i\ ,\ S_j\ ) \qquad \text{eq. 14}$$

where $d_{i,j}$ is the correlation distance between two electrodes i and j. The correlational distance between two electrodes is low when the coordination between them is synchronous, and when they show similar coordination patterns to the rest of the network. First, we used several clustering indices, including Hubert, Silhouette, Davies-Bouldin, Calinski-Harabasz, Hartigan, Homogeneity, and Gap, to find an optimal range of cluster numbers (between 2 and 8 for all subjects) [94–97].

For each cluster number, we ran the K-means algorithm 1000 times. The sample size was subsampled and only 25 percent of electrodes were randomly selected for each clustering (we ensured that each cluster had at least an average of 5 data points). After running the clustering 1000 times, a probability matrix for electrode pairs was defined as the ratio of numbers that electrode pairs clustered together, divided by the number of electrode pairs in the same random sampling for K-Means clustering. This ratio was calculated for all electrode pairs and used to create a matrix of pair-wise grouping probabilities. We then ran a second K-means clustering algorithm on this matrix to identify clusters that were similar in their network-level pair-wise grouping likelihood. Using a similar approach and random sampling of electrodes, we generated another pair-wise grouping probability matrix indicating how often electrodes were clustered

1219 together based on their pair-wise grouping likelihood (**Extended Data Fig. 5e**). Using this
1220 hierarchically defined pair-wise clustering likelihood, we ran a final K-means clustering on all
1221 electrodes, labeling them according to the probability of being stably grouped together for each
1222 cluster number. For each K (cluster number), we calculated clustering accuracy, confusion
1223 (probability of non-diagonal clusters), a confusion rank, and a ratio from dividing median accuracy
1224 (diagonals) by median confusion. We normalized each of the measures between 0 and 1 (1 showing
1225 the best, and 0 showing the worst performance between all clusters). We used these four measures
1226 and in a non-parametric vote, we chose the cluster number that outperformed others in this voting
1227 pool. This non-parametric measure shows how well each K performs to detect more stable clusters
1228 with high accuracy and low confusion level and estimate the optimal number of clusters. While
1229 there is no definitive answer on what number of clusters is the best, we selected the optimal number
1230 of clusters using this method to conduct further analysis. In summary, this clustering technique
1231 reduces clustering biases caused by outlier electrode pairs in all clustering realizations as well as
1232 stabilizes clusters.
1233 To determine whether identified clusters were functionally specialized, we compared their
1234 responses evoked by cues and targets to their baseline activity levels. We calculated the averaged
1235 baseline normalized burst density within windows of 500 ms after cue onset and 750 ms after target
1236 onset. The Wilcoxon test was used to determine if this response was non-zero across the electrodes
1237 in each subnetwork. We corrected for multiple comparisons by using FDR for dependent samples
1238 with an alpha level of 0.05. Clusters that were significantly activated by cue events are referred to
1239 as “cue-subnetworks” and clusters that were significantly activated by target events are referred to
1240 as “target-subnetworks". The cue and target-subnetworks were found in each data set for the
1241 optimal number of clusters. For datasets, for which the optimal number of clusters did not contain

distinct cue and target-subnetworks, if existed, we chose the next K (cluster number) with highest ranking in the clustering measures that contained both subnetworks.

Time-lag analysis between cue and target-subnetworks

We calculated the HFAb-triggered-HFA for pairs of electrodes during the period between the target onset and the manual response to understand how the HFAbs were temporally ordered after the target onset in both the cue and target-subnetworks. Next, we compared HFAb-triggered HFA between electrodes in cue- and target-subnetworks to determine whether there was any asymmetry in the distribution of HFAbs between the two subnetworks. A total of six subjects (3 in experiment 1 and 3 in experiment 2) showed both stable cue and target-subnetworks. We then calculated once the HFAb-triggered HFA when HFA in the target-subnetwork was measured around the HFAbs in cue-subnetworks, and when the HFA in the cue-subnetwork was measured around the HFAbs in target-subnetworks. A lead state was indicated by HFAbs followed by stronger HFA power; a lag state was when HFAbs followed stronger HFA power. First, we measured the maximum asymmetry around the burst onset across all subjects (by calculating the absolute difference between windows of varying lengths, 25 ms to 250 ms every 25 ms). We then calculated the averaged HFAb-triggered-HFA within 150 ms of burst onsets where asymmetry was at its maximum. Next, we asked if the value differed based on the directionality of the two subnetworks. For both directions, we used the Wilcoxon test to determine whether the asymmetry around burst onset is non-zero. Additionally, we tested whether HFAb-triggered HFA differs between the two directions after and before bursts.

For each subject, we visualized the lead/lag interactions between stable cue and target-subnetworks. To achieve a better visualization of lead/lag interactions, we measured the HFA peak

time for each electrode in cue/target-subnetworks relative to HFAb onset across all cluster numbers. Each electrode that was a member of the target-subnetwork or the cue-subnetwork was analyzed to determine its median peak-time-lag relative to the other cluster members. A median peak-time-lag of all electrodes satisfying this condition was then plotted, with red representing a lead, and blue representing a lag (**Fig. 4d, Extended Data Fig. 11c**).

Delayed Mutual Information Analysis. We used mutual information (MI) which is a non-linear metric used in information theory to estimate the shared information between different time segments in two electrodes to find where their mutual predictability is maximized. For each electrode, we extracted data (HFAb density) from -1500 ms to 1500 ms around the target onset (and for the control analysis, around the cue onset). We normalized the data and calculated MI for segments of 750 ms sliding every 50 ms. The MI between electrodes X and Y is given by eq. 15:

$$MI(X,Y)= \sum_{x\in X_w} \sum_{y\in Y_w} p(x,y) \log\left(\frac{p(x,y)}{p(x)p(y)}\right) \qquad \text{eq. 15}$$

where p(x,y) is the joint probability distribution function of each windowed segment of electrodes X and Y, and p(x) and p(y) are their marginal probability distributions. We estimated the probability distribution for each variable and for the joint distributions using a histogram-based approach and binning the data (the number of bins was selected based on the Freedman-Diaconis rule [98] to balance the trade-off between estimation resolution and statistical reliability.

To further quantify how information is directionally coupled between cue and target-subnetworks, we calculated delayed mutual information (DMI). The DMI was calculated by comparing the temporal dynamics and dependencies between these two subnetworks.

The DMI between X and Y was calculated similar to MI, except that one of the timeseries was delayed incrementally to determine whether the past of one electrode is a better predictor of the future of the other electrode. The delay time-lag ranged from -500ms to 500ms with a step of 25ms, as in eq. 16.

$$DMI(X,Y) = \sum_{x \in X_w} \sum_{y \in Y_w^\tau} p(x,y) \log\left(\frac{p(x,y)}{p(x)p(y)}\right) \qquad \text{eq. 16}$$

where X_w is segmented windows of electrode X, and Y_w^τ is segmented windows of electrode Y shifted by a time lag of τ.

The DMI analysis of each electrode pair can inform us about (i) when the electrodes showed maximum inter-predictability relative to an event onset (e.g., target), and (ii) at what time-lag the inter-predictability was maximized. To address this question, we extracted the DMI peaks in a 2D space, which gave us both the time-lag and the timepoint relative to the event onset where two electrodes showed maximum DMI values. We then asked if the time-lag of this peak is different between electrodes in the cue-subnetworks and electrodes in the target-subnetworks. For example, when we shifted the timeseries of electrodes in target-subnetworks, for each electrode in the cue-subnetwork, we measured its mean DMI relative to electrodes in target-subnetworks. We determined at what time lag and at what time relative to target onset DMI was maximized. We used the Wilcoxon test to see if the maximum DMI time-lag (τ_{max}) occurred between electrodes in cue and target-subnetworks was non-zero. The lead and lag patterns in inter-predictability between cue and target-subnetworks were then determined by the sign of the average over τ_{max} for all electrodes in the shifting subnetworks.

Modeling iEEG by spiking neural networks

We investigated high frequency activity in general and high frequency burst events in particular using a limited network of two recording sites placed on two interconnected networks of spiking neurons. For modeling the spiking networks, we used a framework described in [7]. Neuronal point-source models can accurately simulate electrical fields in cortical neural networks [99]. Two cubic neuronal structures were simulated in three dimensions. Synaptic dynamics and connectivity patterns were implemented as explained in [7]. Each cubic network consisted of 1000 neurons (10 x 10 x 10, xyz). We modeled neurons as spherically symmetric points in a 3D grid (with r units on each axis). A recording disk was implemented on top of each network at a distance three times greater than the network depth (**Fig. 5a**). Pairwise connectivity was calculated based on anatomical studies (discussed below) and a distant-dependent Gaussian rule [100,101]. The distant dependent connectivity factor is:

$$P(d) = P_0 \, e^{\frac{-(\frac{d}{r})^2}{\sigma^2}} \qquad eq.17$$

where r is the grid unit, d is the distance between two neurons, σ is the standard deviation of distances between neurons (Barral and Reyes, 2016), and P_0 is a structural scaling factor reflecting the maximum connection probability across the network (see **Supplementary Table 3**).

Four interneuron types were used: Parvalbumin (PV), Calbindin (CB), Calretinin (CR), and Cholecystokinin (CCK) expressing interneurons. Excitatory neurons were divided into regular spiking neurons (70%), intrinsic low-threshold spiking bursting neurons (10%), and fast adapting regular spiking neurons (20%).

Neuron models. We used Izhikevich neuron model [46] for simulating regular spiking, burst spiking, fast spiking and low-threshold spiking neurons. Each neuron is modeled by a series of differential equations as in eq 18.

$$\frac{dv}{dt} = 0.04v^2 + 5v + 140 - u + I \qquad eq.18$$

$$\frac{du}{dt} = a(bv - u)$$

where variables v and u denote neural membrane potential and membrane recovery, respectively. Parameters a and b define the recovery rate and sub-threshold fluctuations sensitivity, respectively. For after-spike resenting the model uses two auxiliary equations as in eq. 19,

$$\text{if } v > 30\ mV \text{ , then } \begin{cases} v = c \\ u = u + d \end{cases} \qquad eq.19$$

the parameter c resets the value of membrane potential v after a spike, and the parameter d adjusts the after-spike recovery variable u. Parameters for different neuron types were chosen as suggested in [102] to approximately generate firing patterns of each neuron type (See **Supplementary Table 4** for each neuron type parameter).

Neural connectivity. Besides distance-based connectivity factors, neuron types had different connection probabilities. We adapted the scaling factor for connectivity between excitatory neurons and inhibitory interneurons from [101]. Additionally, rodent anatomical studies were considered in determining the connectivity among different types of neurons. Generally, PV interneurons inhibit themselves and VIP interneurons (likely similar to CR), whereas SOM interneurons (likely similar to CB) do not inhibit each other, and VIP interneurons disinhibit SOM interneurons preferentially [103,104]. The connectivity between networks was defined by a probability and a rate of connection. This connectivity was attributed primarily to excitatory neurons (90%).

Simulation of post-synaptic potentials. For each neuron the postsynaptic potentials were modeled by a biexponential function as in eq. 20,

$$g(t) = e^{-\frac{t}{\tau_r}} - e^{-\frac{t}{\tau_d}} \qquad eq.20$$

where τ_r and τ_d denote the rise and decay time constant of postsynaptic current, respectively. The biexponential function was implemented through a second-order ordinary differential equation as in eq. 21.

$$\frac{d^2g(t)}{dt^2} = -\frac{(\tau_d + \tau_r)}{\tau_d \tau_r}\frac{dg(t)}{dt} - \frac{g(t)}{\tau_d \tau_r} \qquad eq.21$$

Where t is time relative to spike, and g(t) is the synaptic conductivity. The rise time was set similarly to ~1ms for all neurons while the decay time for pyramidal neurons were and interneurons varied from ~6ms to 24ms [105–108] as shown in **Supplementary Table 4**.

Network external inputs. Each network was fed external currents to generate firing rates similar to cortical neurons. Each neuron received a cosine input. The objective was to first control externally induced rhythmicity in network activation by frequency, as well as phase coherence between the input function and neurons. On average, each network received external input sufficient to generate a 5 Hz firing rate [109]. The external input to pyramidal neurons was three times greater than the external input to inhibitory neurons. In addition, a Brownian noise $(\frac{1}{f^2})$ was added to the input as per previous experimental observations [110].

For nonrhythmic input, we considered slow and ultraslow oscillatory (<1 Hz) input to each neuron with an initial phase lag. Then a coherence index was used to determine the distribution of phase lags among neurons. Thus, the phase range was defined:

$\varphi = 2\pi\ (1 - coherence)$ *eq.* 22

For the rhythmic input, we incrementally increased the cosine input frequency up to 12 Hz for each simulation run. For networks with shared input, we ran 100 simulations in which networks were not connected but received correlated inputs (5-25 percent of neurons received the same input). For networks with feedforward connection, we simulated feedforward networks in which the connections between the two networks are unidirectional. The connectivity strength was changed from 0.001 to 0.1 by one order of magnitude. For each value, we ran 100 simulations. For Networks with reciprocal connections, we fed the networks with uncorrelated inputs, but both networks were reciprocally connected. The connectivity strength was changed by one order of magnitude from 0.001 to 0.1 and the simulation was run 100 times for each value.

To investigate the effect of an external stimuli on directional networks, we simulate a feedforward network as explained before with an internetwork connectivity ratio of 9 to 1 (network 1 and 2 respectively, **Extended Data Fig. 12e**). We then fed network 1 with an external input pulse of 500 ms duration and 250 ms duty cycles (**Extended Data Fig. 12f**). The input was fed to 50 percent of neurons in the network 1. We then calculated the time resolved PLV in both networks as explained before (**Fig. 5i**, **Extended Data Fig. 12g**).

Integration of postsynaptic currents and neural activities at the recording sites. For each simulation, we estimated the field potential at two recording sites (black disks **Fig. 5a**). By assuming neurons as point-source field, we measured field dynamics at each recording site by summing the attenuated membrane potentials and the postsynaptic currents from all neurons. We estimated the voltages at the recording disk by considering membrane and post-synaptic potentials as electrical dipoles (with negligible distance between poles relative to the recording disk). The

electric filed is then represented by $E(r,t)$, where r and t denote the distance from the source and the time, respectively. The extracellular potential is then calculated by:

$$\mathrm{E} = -\nabla V \qquad eq.23$$

Using Ohm's law, the electric field at distance r from each dipole with a current density of I_n (t) is equal to:

$$E(r,t) = \frac{I_n(t)}{4\pi r^3 \sigma} \qquad eq.24$$

with $I_n(t)$ represented as:

$$I_n(t) = I_m(t) + I_{syn}(t) \qquad eq.25$$

where σ denotes the medium conductivity (which we assumed is independent of distance from sources). $I_m(t)$ and $I_{syn}(t)$ are the transmembrane current and the synaptic current of each neuron respectively. By integrating the electric field, we calculated the potential at the disk by:

$$V(r,t) = -\int_{\infty}^{r} E(r',t)dr' = -\int_{\infty}^{r} \frac{I_n(t)}{4\pi r'^2 \sigma}\, dr'$$

$$V(r,t) = \frac{I_n(t)}{4\pi r^2 \sigma} \qquad eq.26$$

The voltage recorded at each site is calculated as in eq 27:

$$V(t) = \frac{1}{4\pi r^2} \sum_{i=1}^{N} \frac{I_n(t)}{r_i} \qquad eq.27$$

where r_i is the distance between the recording disk and the i^{th} point-source, and N is equal to the total number of neurons in each network.

We used a non-ohmic filter to attenuate higher frequencies by getting insights from [111]. We implemented an exponential attenuation in the frequency domain. First for each signal we computed the FFT. We then applied an exponential attenuation factor to the magnitude of the

frequency components (**Extended Data Fig. 12b**). This factor exponentially decreases the amplitude for higher frequencies as in eq. 28:

$$A(f) = e^{-\alpha f} \qquad eq.28$$

Where $A(f)$ is the attenuation factor for frequency f, *and* α is a parameter that controls the rate of exponential decay which we set to 0.01. After multiplying the attenuation factor, we performed the inverse FFT (iFFT) to transform the signal back to the time domain.

For each condition, we ran simulations 100 times, each simulating iEEG signals and neural activity for three seconds. We detected HFAbs at each recording site and calculated the amplitude of the analytical signal as explained in (eq. 1). Next, we examined whether there was a correlation between the density of bursts and the aggregated spike density in each network. The spike density was calculated and smoothed using a Gaussian window of 25 ms. We measured the correlation coefficient between aggregated spike density and burst density for each simulation. On average, burst events were significantly correlated with spike densities in each network.

In a control condition, we randomly assigned burst times and examined the correlation between burst density and spike density. This randomization was performed 1000 times and we found the 95% confidence interval under the null hypothesis that burst density is not related to spike density. All other analyses of the modeling results were conducted in a similar manner to those of the experimental data.

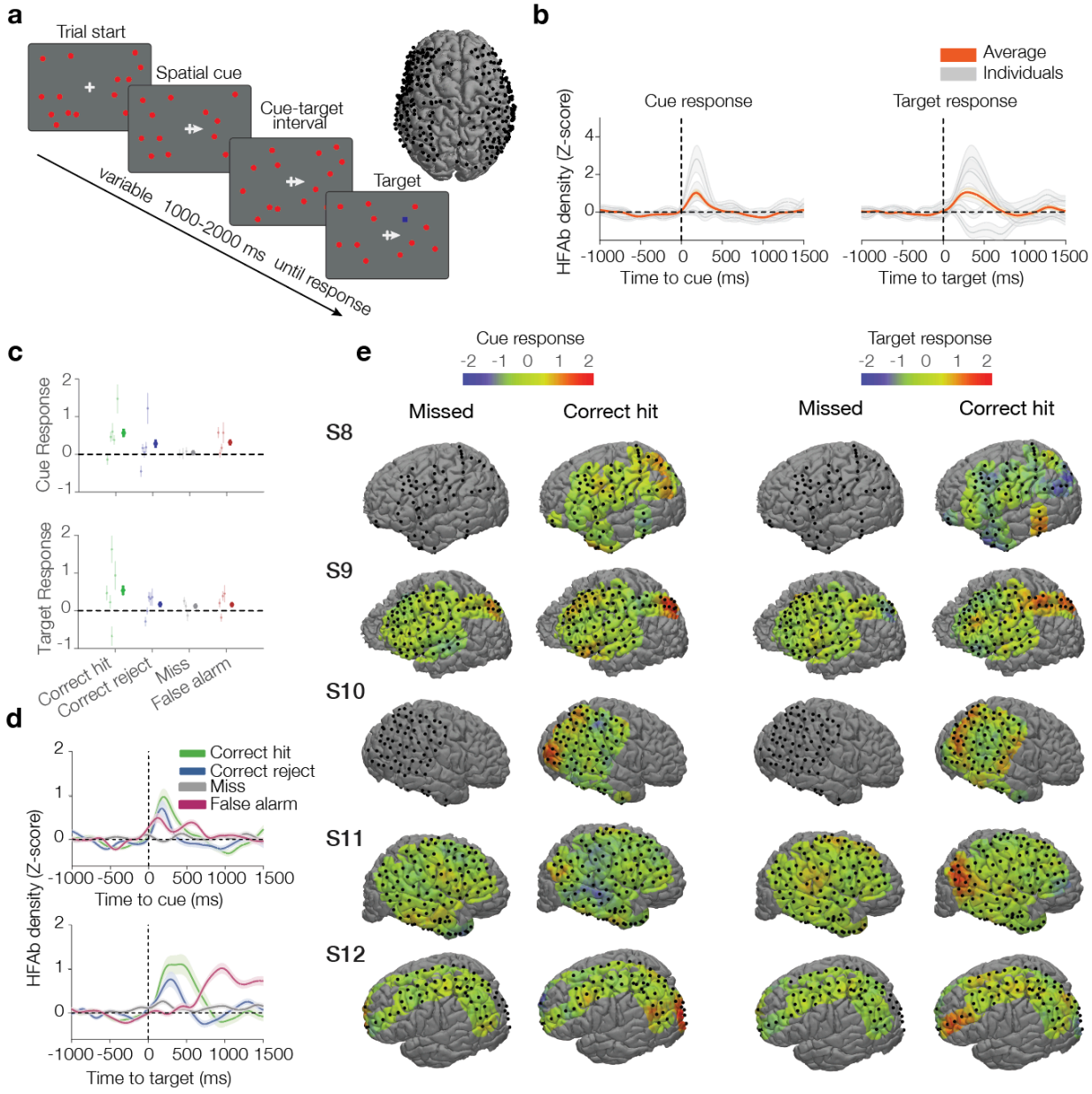

Extended Data Fig. 1. HFAb activation patterns in experiment 2. (**a**) Task structure of experiment 2. Subjects hold their gaze fixation to the center of a screen (a white plus sign) with red circles turning on and off. A spatial cue endogenously cues subject's attention to a hemifield. A target appears at one hemifield and subjects should report whether the target was seen in the cued hemifield. The brain shows the localization of electrodes across all subjects. (**b**) Similar to **Fig. 1b** for experiment 2. (**c**) Similar to **Fig. 1d**, for experiment 2. (**d**) Activation profiles of HFAbs grouped by trial outcome, for experiment 2. (**e**) Similar to **Fig. 1h**, for individual subjects in experiment 2. Participants not having enough incorrect trials for this analysis are not visualized.

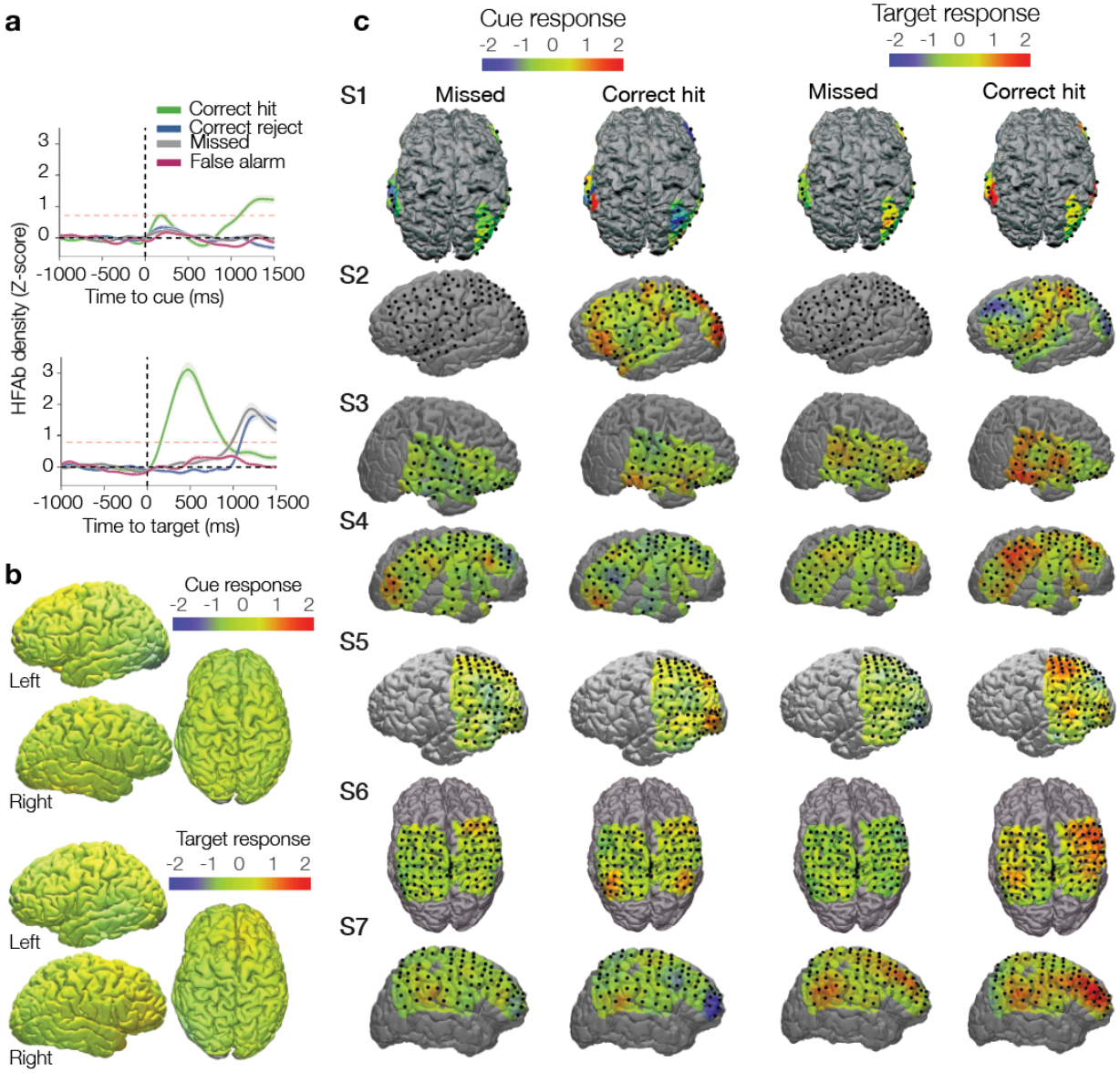

Extended Data Fig. 2. HFAb responses to cue and target events in experiment 1. (**a**) Activation profiles of HFAbs grouped by trial outcome. (**b**) similar to **Fig. 1e, f** for incorrect trials. (**c**) similar to **Fig. 1h**, for individual subjects.

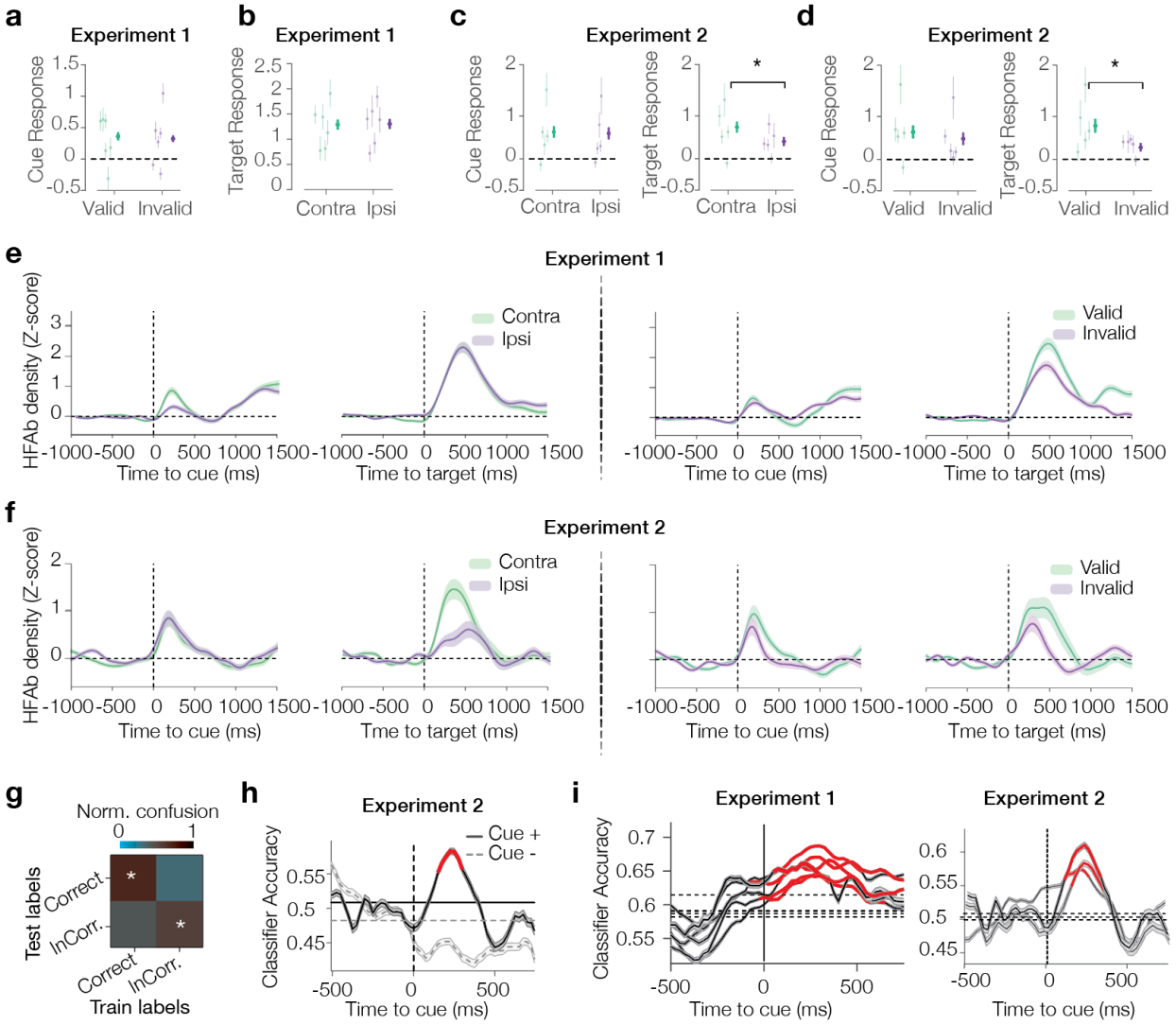

Extended Data Fig. 3. HFAb responses to different experimental conditions in experiment 1 and 2. (**a**) Similar to **Fig. 1I**, showing responses to valid and invalid cues. (**b**) Similar to **Fig. 1j**, showing target responses in trials with cues contra- and ipsi-lateral to the electrode. (**c,d**) Similar plots as in **Fig. 1i,j** for experiment 2 (each line is an individual, error bars are standard errors of the mean, thick lines show average over all subjects). (**e**) Temporal profile of average HFAb density across all subjects and electrodes relative to cue and target onset, for trials with cues contra- and ipsi-lateral to the electrode (left), and for trials with valid or invalid sensory cues (right). (**f**) Similar to E for experiment 2. (**g**) Confusion matrix showing the classifier accuracy (**Fig. 1k**) within 500 ms of cue onset (white asterisks denote significantly higher prediction accuracy than baseline and chance level, binomial test, $P < 0.05$). (**h**) Similar results as in **Fig. 1k** for experiment 2. (**i**) Similar classifier analysis results to **Fig. 1k** when one subject is omitted (each line indicates the result of omitting one subject). Red lines indicate prediction accuracy higher than baseline (dashed lines) and chance levels (binomial test, $P < 0.05$, FDR corrected for dependent samples). Shaded error bars indicate the standard error of the mean across all realizations and cross validations.

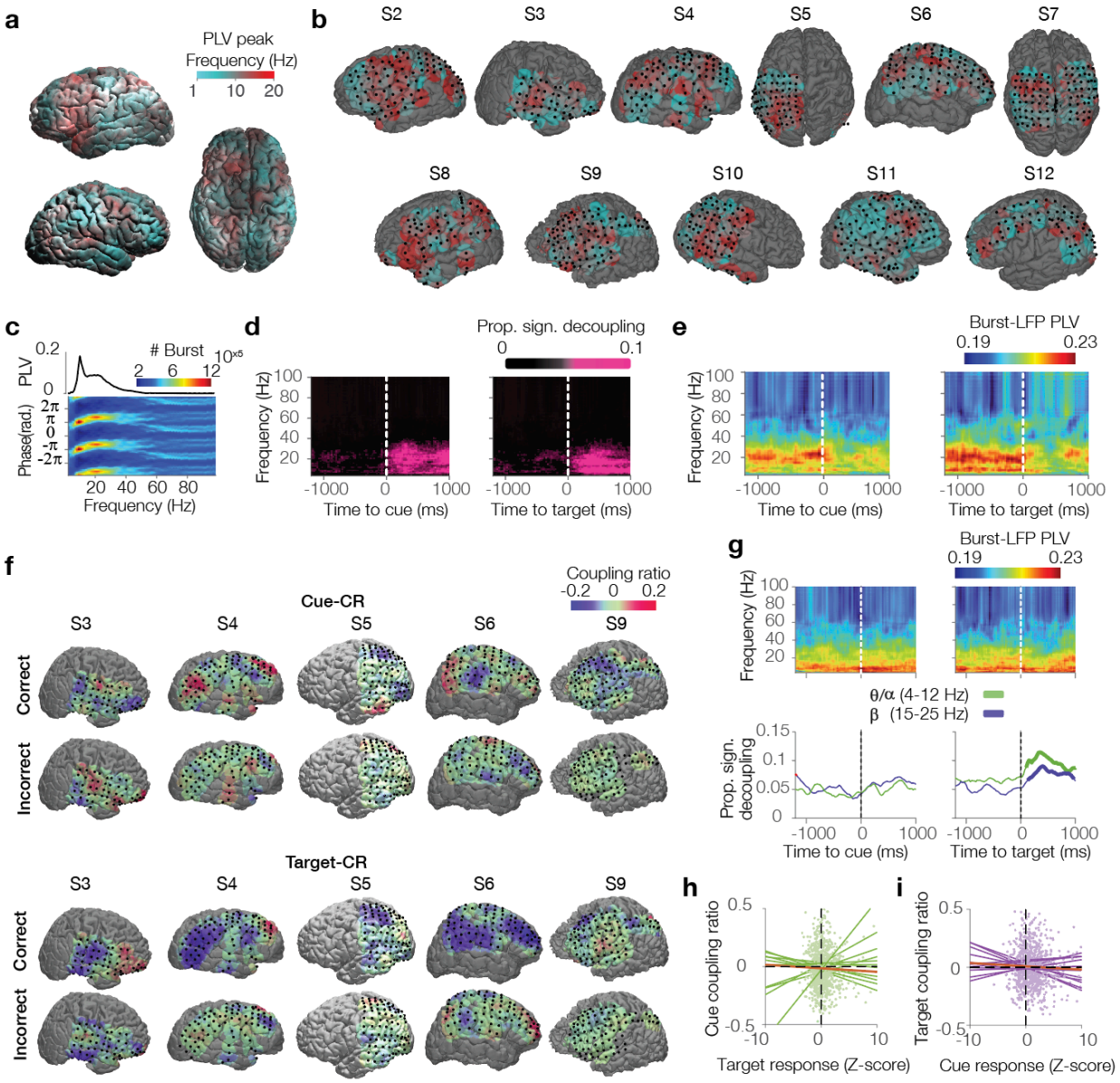

Extended Data Fig. 4. HFAb coordination with low frequency activity in experiment 1 and 2. (a) Group level average spatial pattern of observed frequency peak of HFAb phase locking to LFP. (**b**) Individual examples showing the spatial pattern of the observed frequency peaks of the HFAb phase locking to LFP. (**c**) An individual electrode example of the phase-frequency distribution of HFAbs locked to both theta/alpha and beta frequency bands. (**d**) Corresponding to **Fig. 2e**, showing the proportion of time-frequency points where phase locking was significantly lower than baseline ($P < 0.05$, random permutation test). (**e**) Similar to **Fig. 2e**, but after removing event-related potential from the LFP (see **Methods**). (**f**) Examples of the coupling ratio between HFAb and low frequency (4-25 Hz) LFP following cue and target onsets in correct and incorrect trials. (**g**) Similar to **Fig. 2e** for experiment 2. (**h,i**) Regression plots showing correlation of coupling ratios following cue onset with target responses (green, **h**), and coupling ratios following target onset with cue responses (purple, **i**). Scatter points denote electrodes, lines indicate individual subjects with orange line showing the regression across all subjects.

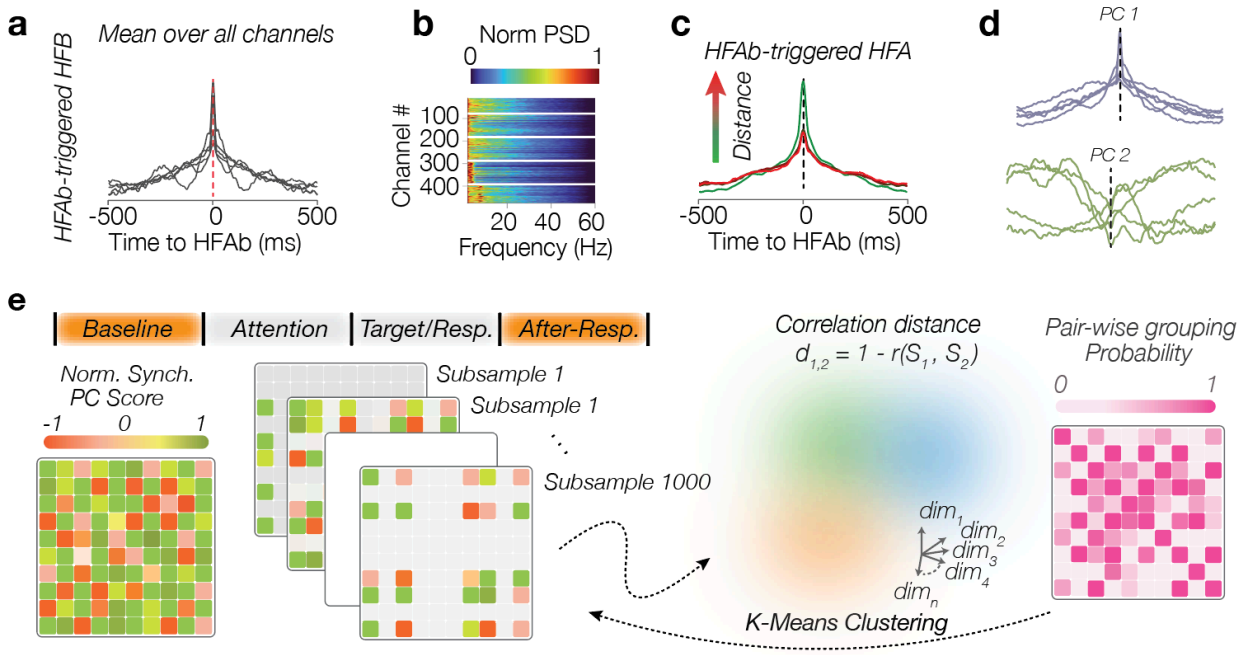

Extended Data Fig. 5. A network clustering approach based on the coordination of HFAbs between electrodes. (a) The average HFAb-triggered HFA for individuals in experiment 2. (**b**) The normalized PSD for HFAb-triggered HFA in experiment 2**. (c)** HFAb-triggered HFA for electrodes distanced in 4 different quantiles (25,50, 75, 100 mm), ranging from green (short) to red (long) in experiment 2, similar to **Fig. 3c**. (**d**) The first and second principal components of HFAb-triggered HFA for individual subjects in experiment 2. (**e**) A schematic demonstration of network clustering algorithm. We used HFAbs outside of cue/delay and target/response periods. The network synchrony matrix shows the loading values for each electrode pair on the synchronized component. A K-means clustering was performed on randomly selected electrode samples for different cluster numbers (K = 2 to 8). We calculated a pair-wise grouping probability matrix in which each element indicates how likely it is that two electrodes will be grouped together. The next step was clustering with network subsampling, similar to the previous step but based on the pairwise grouping likelihood matrix. The final clustering of the pair-wise grouping likelihood results indicated stable clusters for each K (see **Methods**).

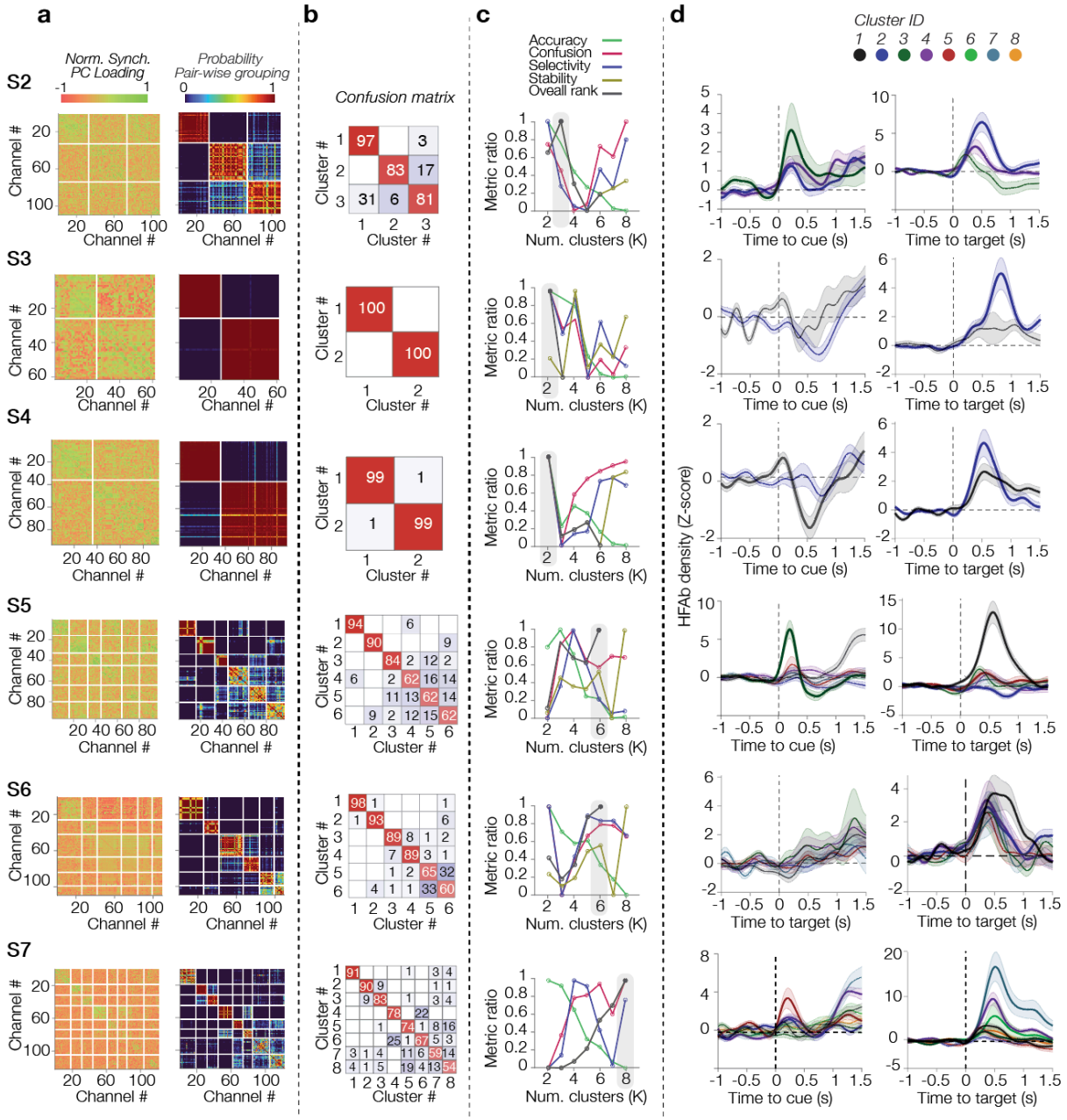

Extended Data Fig. 6. Clustering results for individual subjects in experiment 1. (**a**) For each subject, the square matrix shows color-coded loading values on the synchronized PC (left) and the pairwise grouping probability (right). (**b**) The confusion matrix for the optimal number of clusters. The diagonals show the average percentage of cluster members grouped together across all clustering over subsamples. The non-diagonals indicate the percentage of members in one cluster who were confused with members in another cluster across all clustering over subsamples. (**c**) Optimal number of clusters is selected using four metrics and a nonparametric voting rank metric (black). The accuracy is determined by the median diagonals, the confusion by the median nondiagonal, selectivity by the relative rank of the diagonal over the highest nondiagonal rank, and stability by the relative rank of the diagonal over the nondiagonal rank. (**d**). Similar to **Fig. 3g** for different subjects. Shaded error bars indicate the standard error of the means, thicker lines indicate significant functional subnetworks.

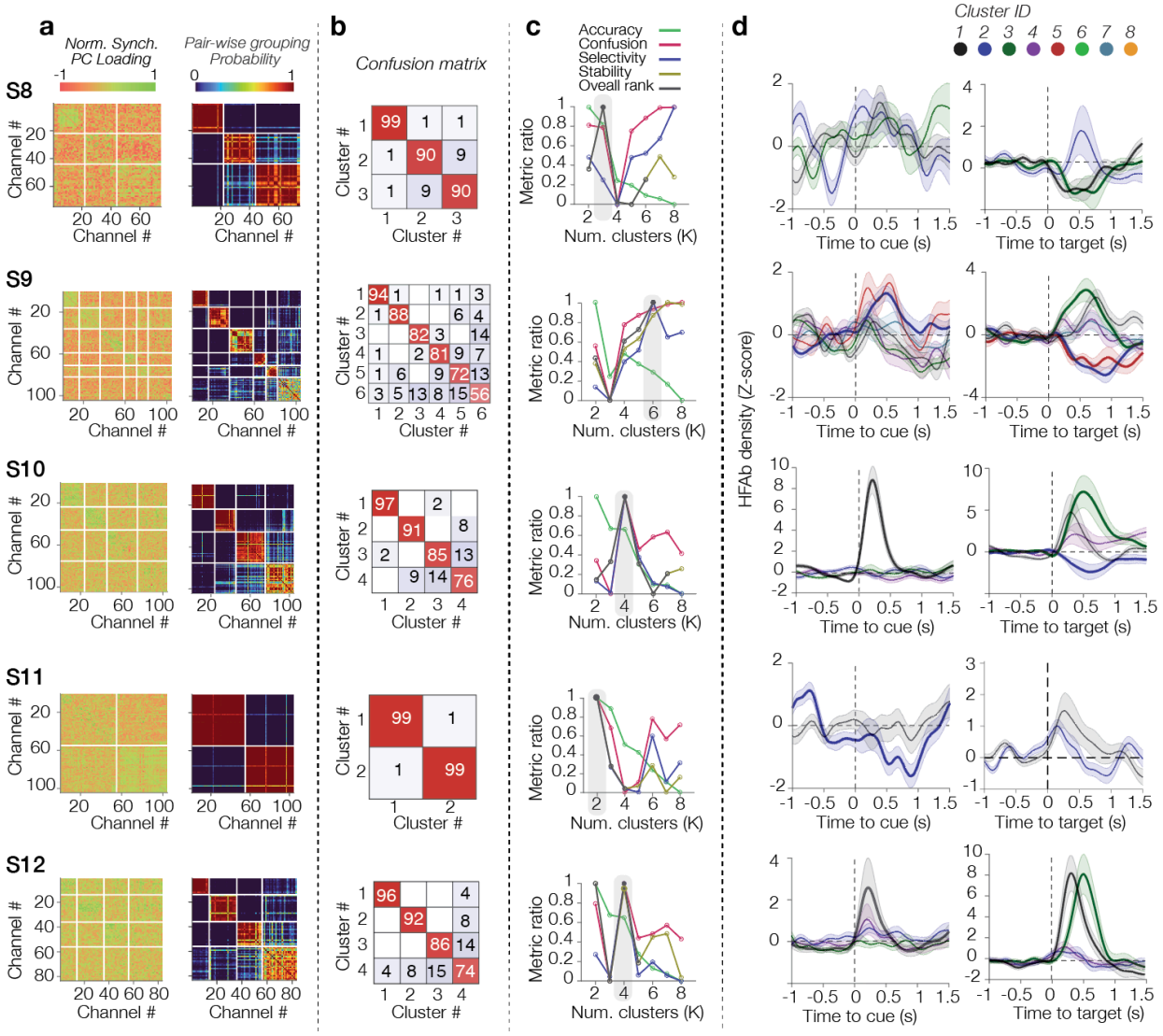

Extended Data Fig. 7. Clustering results for individual subjects in experiment 2. (**a-d**) Similar to **Extended Data Fig. 6. a-d** for experiment 2.

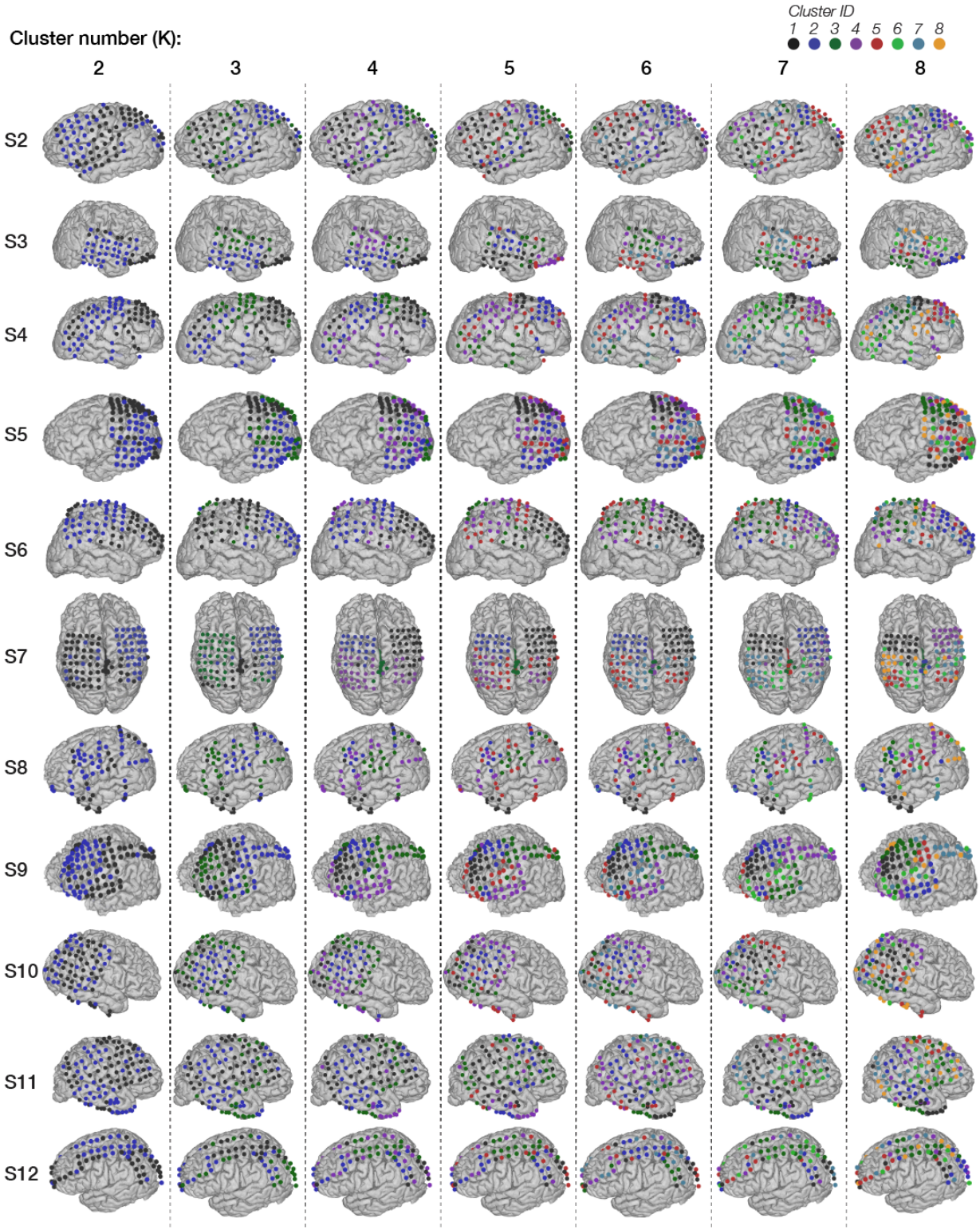

Extended Data Fig. 8. Organization of clusters based on cluster numbers. Columns from left to right show the results for cluster numbers K = 2 - 8. The cluster IDs are sorted by cluster stability.

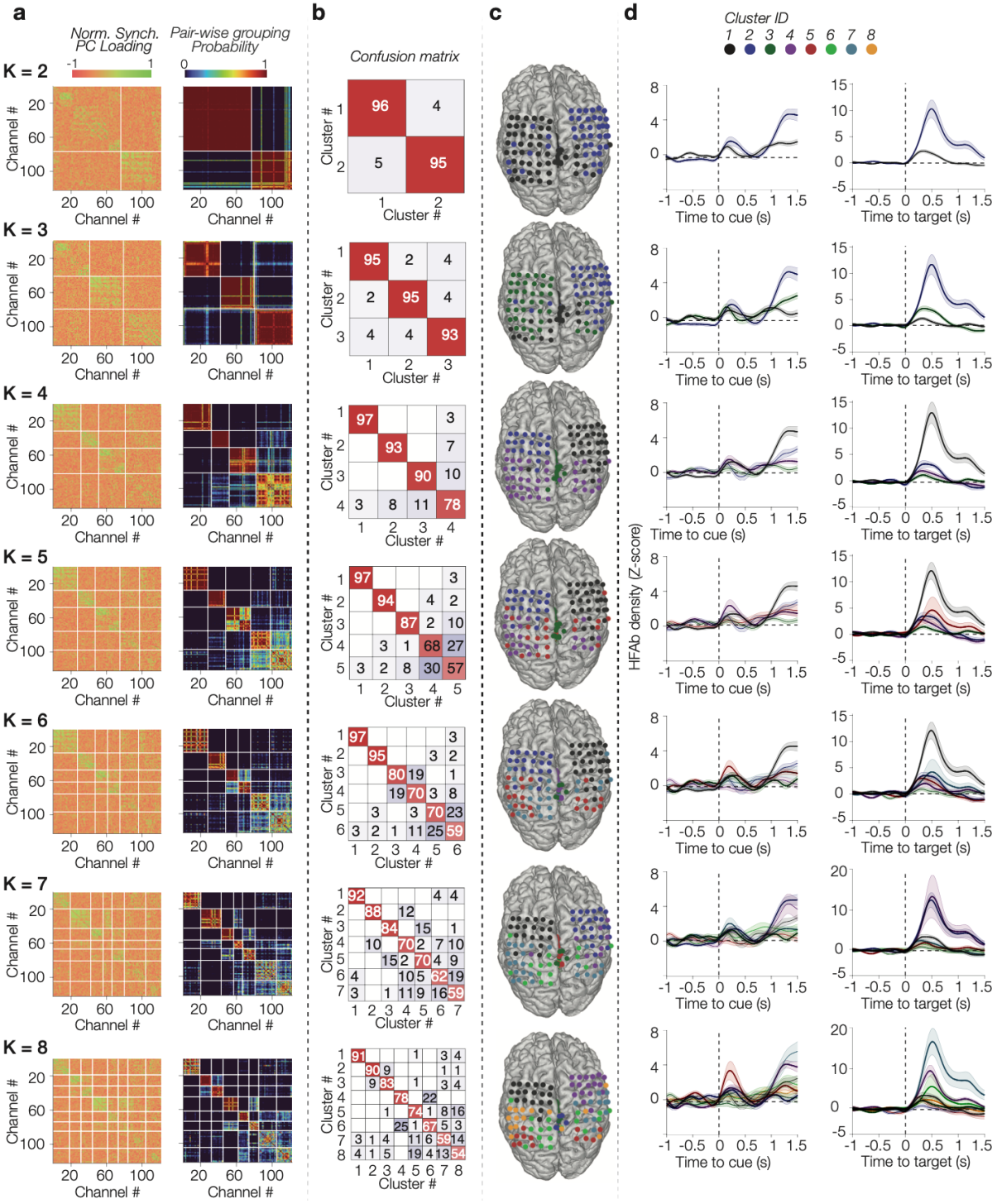

Extended Data Fig. 9. Results for different cluster numbers for an individual subject. (**a**) Similar to **Extended Data Fig. 6a** for different Ks. (**b**) Confusion matrices for different Ks. (**c**) Cluster topography for different Ks. (**d**) Similar to **Extended Data Fig. 6d** for different Ks.

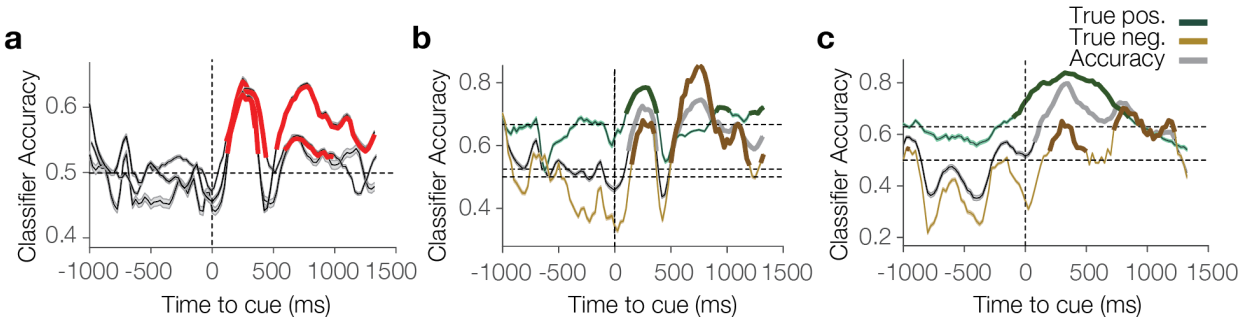

Extended Data Fig. 10. Classifier trained on cue-subnetworks predicts outcome. (**a**) As in **Fig. 3h**, each line represents classifier results when one subject is omitted. (**b, c**) Classifier accuracy in predicting correct trials (green), errors (brown), and the average accuracy (gray) for (**b**) experiment 1 and (**c**) experiment 2. The shaded error bars show the standard error of the mean. Thick lines indicate timepoints where the accuracy of the prediction is significantly higher than the baseline (dashed lines) and chance level ($P < 0.05$, binomial test, FDR corrected for dependent samples).

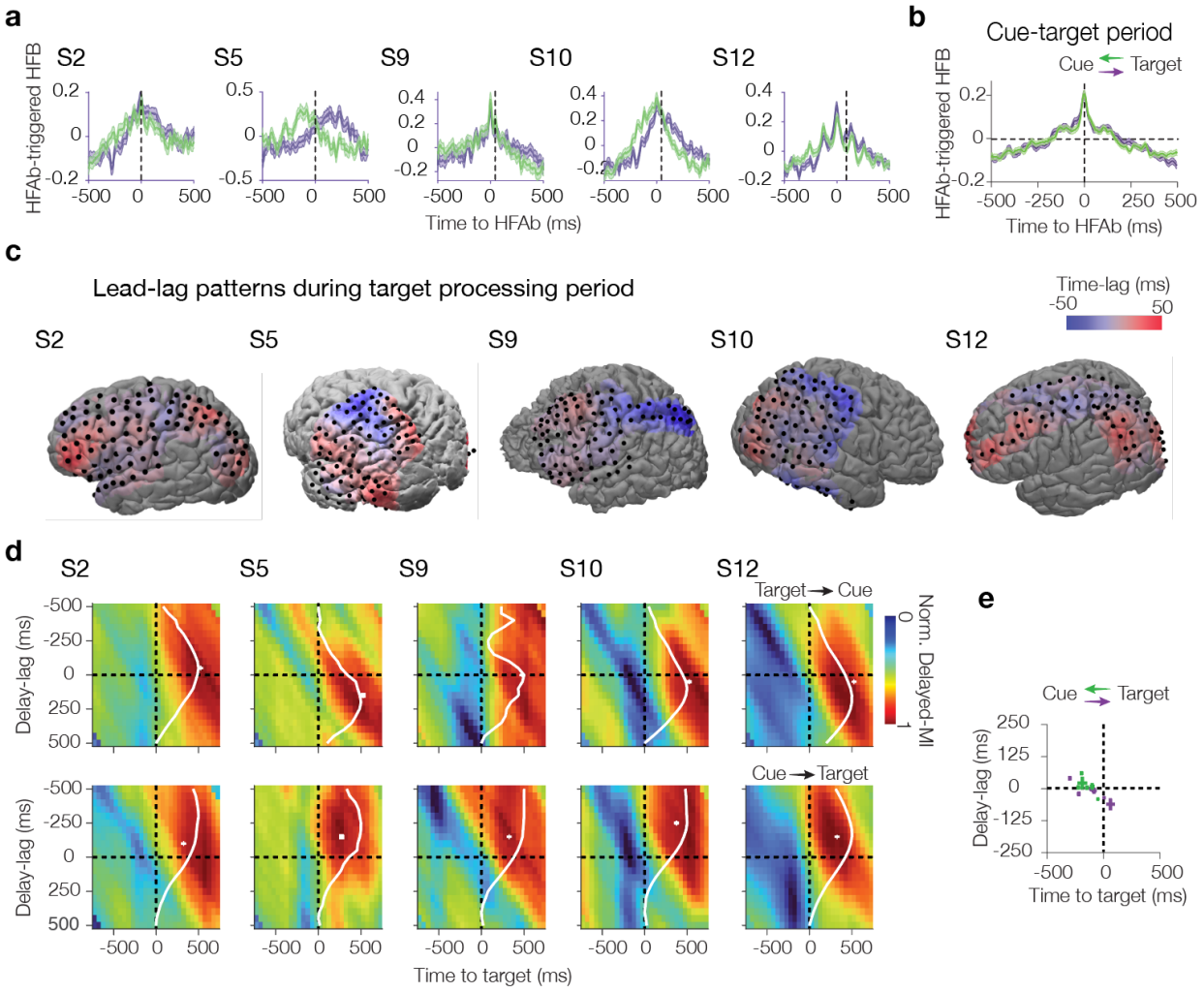

Extended Data Fig. 11. Temporal precession between cue and target-subnetworks. (**a**) HFAb-triggered HFA examples for individual subjects similar to **Fig. 4a**. (**b**) Group-level average of HFAb-triggered HFA, similar to **Fig. 4b**, but for HFAbs during the cue/delay period. (**c**) Visualization of lead-lag patterns across members of the cue and target-subnetworks during target processing for all clusters (similar to **Fig. 4d**). (**d**) DMI results for individual subjects similar to **Fig. 4e**. (**e**) similar to **Fig. 4g**, around the cue onset.

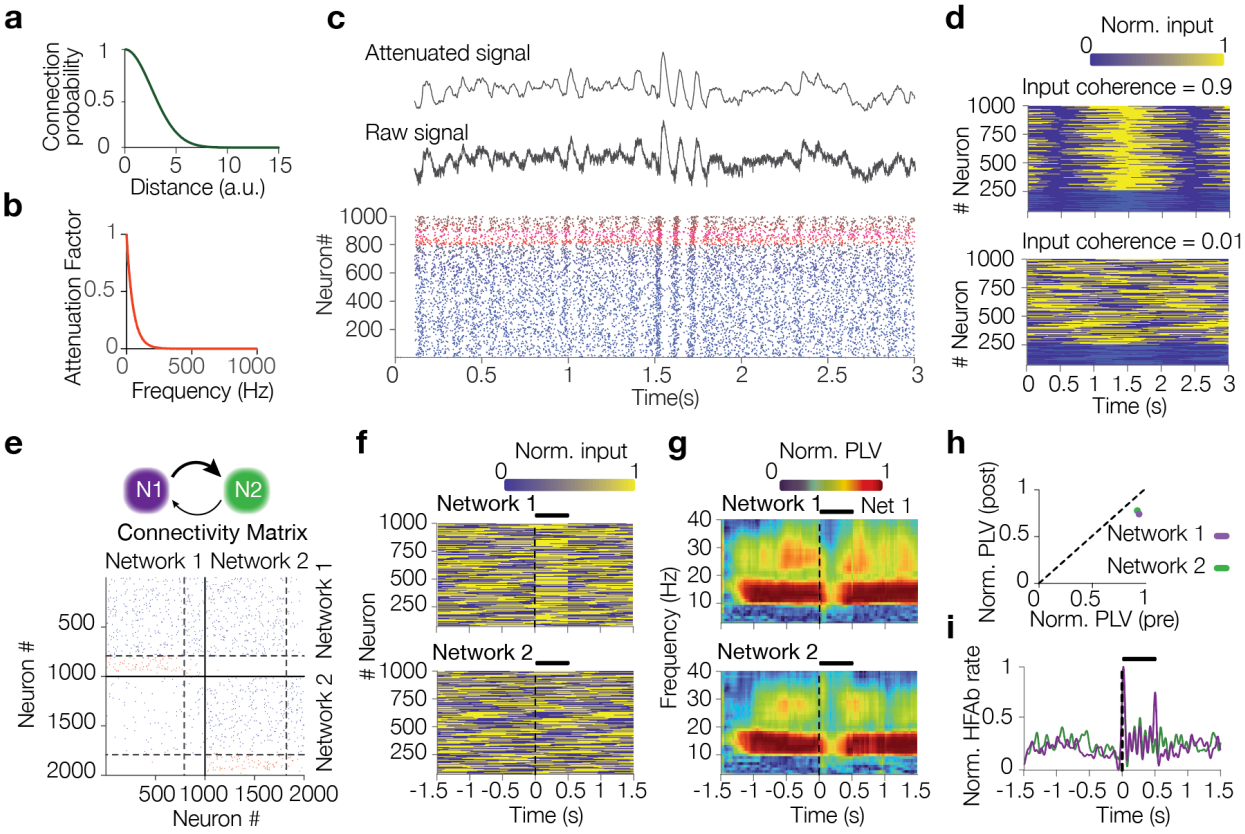

Extended Data Fig. 12. Computational modeling of iEEG signal. (**a**) A factor that scales the connection probability between neurons in each network as a function of their distance. (**b**) A factor used to attenuate high frequency activity in iEEG signals. (**c**) A complete trial simulation example. Rasters show the activity of neurons in one network (bottom, blue and red show excitatory and inhibitory neurons, respectively). Raw and attenuated traces correspond to field dynamics of the same network. (**d**) Ultra slow inputs to one network when inputs to neurons have coherent (top) and random (bottom) phases. (**e**) Detailed network structure for simulating a directional network with stronger input from network 1 to network 2 (each scatter point indicates whether two neurons have excitatory (blue) or inhibitory (red) connections). (**f**) An input design evaluating how a transient stimulus affects HFAb coherence with LFP in a network as shown in E (network 1 (top) receives a transient coordinated input). (**g**) Similar to **Fig. 5I**, showing PLV changes in both networks by transient input. (**h**) In both networks 1 and 2, the PLV drops within 500ms of stimulus onset ($P < 0.001$, Wilcoxon test). (**i**) Normalized burst rate relative to stimulus onset.

Supplementary Tables

Subject ID	Cue +	Target +
S1	IFG, TPJ, V3b, hV4	ISP0, MFG, MTG, TPJ
S2	Cingulate Gyrus, ISP2, IFG, IPL, LO2, MFG, Postcentral Gyrus, SFG,	Cingulate Gyrus, ISP1, ISP3, IPL, MFG, Paracentral Lobule, Postcentral Gyrus, Precentral Gyrus, SFG, STG
S3	IPL	IFG, IPL, ITG, MTG, Orbital Gyrus, Precentral Gyrus, SFG, STG, TPJ
S4	IPL, MFG, hMT, Postcentral Gyrus, LO2	Angular Gyrus, FEF, FFG, IFG, IPL, MFG, Postcentral Gyrus, Precentral Gyrus, SFG, STG, TPJ,
S5	FFG, ISP2, ISP3, LO2, MOG, MTG, Postcentral Gyrus, hMT	FEF, FFG, IPL, MTG, Postcentral Gyrus, Precentral Gyrus, SFG, TPJ
S6	FEF, IPL, Postcentral Gyrus, SFG, TPJ	FEF, IPL, MFG, Paracentral Lobule, Postcentral Gyrus, Precentral Gyrus, Precuneus, SFG, STG, TPJ
S7	ISP2, ISP3, IPL, Postcentral Gyrus, SFG, SPL, TPJ	FEF, ISP2, ISP3, ISP5, IPL, Paracentral Lobule, Postcentral Gyrus, Precentral Gyrus, Precuneus, SFG, SPL, TPJ
S8	LO1	FEF, ISP1, ISP2, MFG
S9	ISP2, ISP3, MFG, STG	ISP1, ISP2, ISP3, MFG, MTG, Precentral Gyrus, SFG, STG
S10	ISP2, ISP3, MFG, Postcentral Gyrus, FEF	FEF, ISP2, ISP3, IFG, IPL, MFG, MTG, Postcentral Gyrus, Precentral Gyrus, SFG, STG
S11	ISP2, MFG, hV4	ISP1, ISP2, ISP3, IFG, MFG, MTG, Postcentral Gyrus, STG
S12	ISP2, ISP3, Postcentral Gyrus	FEF, ISP1, ISP2, ISP3, IPL, MFG, MTG, Postcentral Gyrus, Precentral Gyrus, SFG

Supplementary Table 1. List of brain areas containing electrodes that showed significant HFAb response to cue (cue +) and target (target +, see **Methods**). The abbreviations are: Inferior Frontal Gyrus (IFG), Temporoparietal Junction (TPJ), Visual area 3b (V3b), human Visual area 4 (hV4), Intraparietal Sulcus (IPS1, IPS2, IPS3, IPS5), Middle Frontal Gyrus (MFG), Middle Temporal Gyrus (MTG), Inferior Parietal Lobule (IPL), Lateral Occipital area 2 (LO2), Superior Frontal Gyrus (SFG), Superior Temporal Gyrus (STG), Inferior Temporal Gyrus (ITG), Frontal Eye Field (FEF), Fusiform Gyrus (FFG), Inferior Occipital Gyrus (IOG), Parahippocampal Gyrus (PHG), Middle Occipital Gyrus (MOG), human Middle Temporal/V5 (hMT), Superior Parietal Lobule (SPL), and Lateral Occipital area 1 (LO1).

Subject ID	Cue Subnetworks	Target Subnetworks
S2	Cingulate Gyrus, ISP2, ISP3, IFG, IPL, MTG, Paracentral Lobule, Postcentral Gyrus, Precentral Gyrus, STG	Cingulate Gyrus, ISP1, ISP2, ISP3, IFG, IPL, MFG, MTG, Paracentral Lobule, Postcentral Gyrus, Precentral Gyrus, SFG, STG
S3		IFG, IPL, ITG, MFG, MTG, Postcentral Gyrus, Precentral Gyrus, STG, TPJ
S4		Angular Gyrus, Anterior Cingulate, Cingulate Gyrus, FEF, FFG, IFG, IOG, IPL, ITG, MFG, MTG, PHG, Postcentral Gyrus, Precentral Gyrus, SFG, STG, TPJ
S5	FFG, LO2, MOG, Postcentral Gyrus, hMT	FEF, IPL, Postcentral Gyrus, Precentral Gyrus, SFG
S6		FEF, ISP2, ISP3, IPL, MFG, Paracentral Lobule, Precentral Gyrus, Precuneus, SFG, STG, TPJ
S7	ISP2, ISP3, ISP5, IPL, SPL, TPJ	FEF, ISP2, ISP3, ISP5, IPL, Paracentral Lobule, Postcentral Gyrus, Precentral Gyrus, Precuneus, SPL, SFG, TPJ
S8		FEF, ISP1, ISP2, MFG
S9	ISP1, ISP2, ISP3, MFG, STG	ISP1, ISP2, ISP3, MFG, MTG, Precentral Gyrus, SFG, STG
S10	FEF, ISP2, IPL, MFG, Postcentral Gyrus, Precentral Gyrus, SFG, STG	FEF, ISP2, IFG, IPL, MFG, MTG, Postcentral Gyrus, Precentral Gyrus, SFG, STG, TPJ, V3b
S11	ISP1, ISP2, ISP3, MFG, Postcentral Gyrus, Precentral Gyrus	FEF, ISP1, ISP2, ISP3, IFG, IPL, MFG, MTG, Postcentral Gyrus, Precentral Gyrus, SFG, STG

Supplementary Table 2. List of brain areas containing cue- and target-activated subnetworks (see **Methods**). The abbreviations are: Intraparietal Sulcus (IPS1, IPS2, IPS3, IPS5), Inferior Frontal Gyrus (IFG), Inferior Parietal Lobule (IPL), Middle Temporal Gyrus (MTG), Superior Temporal Gyrus (STG), Middle Frontal Gyrus (MFG), Superior Frontal Gyrus (SFG), Inferior Temporal Gyrus (ITG), Temporoparietal Junction (TPJ), Frontal Eye Field (FEF), Fusiform Gyrus (FFG), Inferior Occipital Gyrus (IOG), Parahippocampal Gyrus (PHG), Middle Occipital Gyrus (MOG), Visual area 3b (V3b), Superior Parietal Lobule (SPL), and human Middle Temporal/V5 (hMT).

Cell-type	Pyr	PV	CCK	CB	CR
Pyr	0.3	0.5	0.5	0.5	0.5
PV	0.6	0.4	0.25	0.15	0.05
CCK	0.6	0.25	0.4	0.15	0.05
CB	0.6	0.6	0.6	0.05	0.25
CR	0.05	0.05	0.05	0.6	0.05

Supplementary Table 3. Connectivity strength between neuron types in each network (see **Methods**).

Cell-type / Parameters	Pyr	PV	CCK	CB	CR
population	0.76	0.07	0.02	0.9	0.06
a	0.02	0.1	0.05	0.02	0.02
b	0.2	0.23	0.23	0.23	0.23
c	-65	-65	-65	-65	-65
d	8	2	2	2	2
τ_r	1	1	1	1	1
τ_d	6.4	8	12.4	16	16

Supplementary Table 4. Parameters used for modeling different neuron types. The parameter a indicates a recovery rate variable, b the sensitivity to sub-threshold fluctuations, c the membrane potential, d adjusts the after-spike recovery variable, τ_r synaptic potential rise time, and τ_d synaptic potential decay time (see **Methods**).